Polymer Bulletin
https://doi.org/10.1007/s00289-019-02893-x

ORIGINAL PAPER

# Investigation on enhancement of electrical, dielectric and ion transport properties of nanoclay-based blend polymer nanocomposites

**Anil Arya**[1] · **A. L. Sharma**[1]

Received: 30 May 2019 / Revised: 18 July 2019 / Accepted: 24 July 2019
© Springer-Verlag GmbH Germany, part of Springer Nature 2019

## Abstract

An intercalated blend polymer nanocomposite (PNC) films based on blend (PEO–PVC), $LiPF_6$ as salt and modified montmorillonite (MMMT) as nanoclay are prepared via solution cast method. The impact of the nanoclay on the morphology, structure, polymer–polymer, polymer–ion interactions, ionic conductivity, voltage stability window, glass transition temperature, dielectric permittivity, and ac conductivity has been explored. The structural analysis evidenced the formation of blended and intercalated polymer nanocomposites. The FTIR analysis confirmed the interaction between polymer–ion-nanoclay, and polymer intercalation is evidenced by the out-of-the-plane mode [Si–O mode] of MMMT. An increase in the fraction of free anions with clay addition is confirmed. The highest ionic conductivity of about ~ $8.2 \times 10^{-5}$ S $cm^{-1}$ (at RT) and $1.01 \times 10^{-3}$ S $cm^{-1}$ (at 100 °C) is exhibited by 5 wt% MMMT based PNC. A strong correlation is observed between the glass transition temperature, crystallinity, melting temperature ($T_m$), ionic conductivity, relaxation time, and dielectric strength. The dielectric data have been fitted and enhanced dielectric strength and lowering of the relaxation time ($\tau_{\varepsilon'}$ and $\tau_m$) with clay addition evidences the faster segmental motion of polymer chain. The intercalated PNC shows thermal stability up to ~ 300 °C, high ion transference number (~ 1), and broad voltage stability window of ~ 5 V. An absolute agreement between ion mobility ($\mu$), diffusion coefficient ($D$), and ionic conductivity is observed. An ion transport mechanism has been proposed on the basis of experimental results. Therefore, the proposed PNC can be adopted as electrolyte cum separator for energy storage devices.

**Keywords** MMMT · Impedance spectroscopy · Transport parameters · Li-ion battery

✉ A. L. Sharma
alsharma@cup.edu.in

[1] Department of Physical Sciences, Central University of Punjab, Bathinda 151001, India

Published online: 30 July 2019

## Introduction

In order to fulfill the environmental norms and choking of global warming, the development of sustainable and renewable energy resources remains a major challenge for the energy sector scientific community. The most convenient and promising source of energy that has been explored is the Li-ion batteries (LIBs) and has revolutionized the energy sector as well as fulfill the energy demand all over the world for application in household appliances, electric vehicles, agriculture, and portable electronic devices. The LIBs possess various advantages such as lighter in weight, economic, no memory effect, high cycle stability (> 5000), high energy efficiency (> 90%), and low redox potential (− 3.04 V vs. SHE) [1–3].

In 1978, Armand [4] proposed the approach of a battery that comprises two electrodes with different potential and Li-ion flows in between them termed as rocking chair battery. The world's first commercial prototype LIB was introduced in 1991 by the SONY Corporation and comprises of an anode (positive electrode; made of graphite), the cathode (negative electrode; made of lithium), and liquid electrolyte poured separator [5]. The liquid electrolyte has a drawback as it may fire up the battery due to leakage or flammable nature and violent reactions may occur in the open environment. Addition of ionic liquid and plasticizer resolved a little bit of the leakage issue. Nevertheless, poor mechanical and dimensional stability remain a key drawback [6]. The solution to the above-said issue is the development of all-solid-state batteries (ASSBs) based on a solid electrolyte that will improve the safety limit of operation, durability and prevents electrolyte leakage. The solid electrolyte can be used in the Li-ion batteries as an alternative to the liquid electrolyte. The desirable properties for a solid polymeric separator are, it must possess the value of ionic conductivity ($\geq 10^{-4}$ S cm$^{-1}$), low glass transition temperature (− 30 to 55 °C), negligible elecronic conductivity ($\leq 10^{-10}$ S cm$^{-1}$), high ion transference number ($t_{ion} \sim 1$), appropriate chemical compatibility with electrode, high thermal stability, flexibility and a wide electrochemical window (≥ 4 V) are necessary [7]. The unique advantage of the free-standing solid electrolyte may be seen as it may serve the dual purpose as it could act as an electrolyte as well as a separator. Its benefits may directly be observed as it may reduce the size, weight, and more importantly, cost for safe and durable high energy density rechargeable batteries.

Nowadays, polymers have been more frequently adapted as the host matrix due to the growing demand for flexible devices. The property on the selection of host polymer comprises of high molecular weight, low glass transition temperature, and least cohesive energy. The electron-rich group (polar group; –O–, –N–, –S, C=O, C≡N) in the polymer host provides the coordinating sites for cation migration, while anion seems to be hanging with the polymer backbone. The first report on the polymer electrolyte was launched in the 1970s, and Fenton et al. [8] in 1973 published the report that deals with ion conduction via polymer matrix. Then in 1978, the practical aspects based on polymer electrolytes were proposed by Armand. The advantages associated with polymer electrolytes are varied shape geometries, desirable flexibility, thin film forming ability, lighter weight, ease of

preparation and cost-effective and make them a promising candidate. The polymer electrolytes eliminate the need for the organic solvents and prevent short circuiting that may explode the battery. The utmost frequently used host polymer in solid polymer electrolytes are PEO, PVC, PPO, PVP, PMMA, and PAN and out of them, polyethylene oxide (PEO) has grabbed the attention of researchers due to its flexibility, the presence of ether group, low glass transition temperature and easy availability [9, 10]. However, the semicrystalline nature of PEO prevents its use due to low ionic conductivity. Various approaches are adopted to improve the ionic conductivity, e.g., cross-linking, hybrid electrolyte, and polymer blending. Among them, polymer blending is a cost-effective method and has received more attention due to improved properties of the blend as compared to both polymers. The blend polymer results in the structural alteration of the host polymer matrix and lowers the crystalline tendency of the host polymer. The possible interaction in blend polymer is (1) dipole–dipole interactions, (2) hydrogen bonding, and (3) ionic interactions. A number of the blend polymers are reported such as PAN, PEMA, PVP, and PVC. Polyvinyl chloride (PVC) is the interesting candidate to be chosen for blending due to high amorphous content which helps in reducing the crystallinity of PEO and improving the ionic conductivity [11].

The $LiPF_6$ has been chosen as salt due to its good ionic conductivity (7.9 mS $cm^{-1}$; 1 M), the smaller cation size (~0.76 Å), the bulky anion (~2 Å), and good solubility. The other advantage with $LiPF_6$ is that it provides the proper balance of properties that strengthens its candidature as well as it provides the formation of proper solid electrolyte interface (SEI) on graphite anode and a protective layer on the aluminum current collector. Other salts with a large anion such as LiTf, LiFSI, LiTFSI, and LiBETI are also available, but corrosion with the aluminum collector, poor solubility, and higher cost limits their use in commercial devices [5, 12–14].

The various approaches have been employed to enhance the prerequisite property of solid polymer electrolyte consisting of polymer (individual polymer/more than one polymer) and salt but failed to achieve the adequate value due to the dominance of concentration polarization. In order to minimize the concentration polarization various route have been explored like: micro/nanofiller dispersion, incorporation of different organophilic nanoclay. The incorporation of organophilic nanoclay seems fit in order to eliminate the concentration polarization arising due to the presence of both cation and anion in the matrix [6, 15–17]. In our previous study, we adopted the dispersion approach using the $TiO_2$ as nanofiller in the PEO–PVC + $LiPF_6$ blend matrix [18]. So, a continuation of the previous studies on the polymer nanocomposites, we prepared intercalated polymer nanocomposites using layered MMMT as nanoclay (inorganic filler) with PEO–PVC as the host matrix. Despite the above advantage, MMMT has low cost, easy intercalation capability and good chemical compatibility [19]. The presence of the surface negative charge on the MMMT clay galleries effectively separates the cation and anion and improves the electrical conductivity ($\sigma = \sum n_i z_i \mu_i$ where $n_i$, is, and $\mu_i$ refer to a number of charge carriers, ion charge, and ion mobility, respectively) [20]. Polymer intercalation is a thought-provoking approach and plays a key role in (1) suppressing the concentration polarization by avoiding anion mobility, (2) enhancement of the ion migration by allowing the cation-coordinated polymer chain confinement in clay galleries, and (3) cation

charge on clay surface acts as Lewis acid and competes with $Li^+$ cation to form complex with polymer which reduces ion coupling [16, 21]. There are various reports on the polymer–clay nanocomposites based on PEO, PAN, PVC, PMMA, PVdF-HFP, and copolymers [22–26].

An attempt has been made to understand the effect of polymer intercalation and to build a correlation between the bulk conductivity, melting point, transport parameters, and relaxation time. In this paper, an intercalated polymer nanocomposite comprising of PEO–PVC as a blend polymer matrix, lithium hexafluorophosphate ($LiPF_6$) as salt, and dodecyl-modified montmorillonite (MMMT) as intercalant has been investigated. The highest electrical conductivity is about ~ $8.2 \times 10^{-5}$ S $cm^{-1}$ (at RT) and increases to $1.01 \times 10^{-3}$ S $cm^{-1}$ (at 100 °C) for 5 wt% MMMT. The impedance results are also supported by various parameters, activation energy ($E_a$), melting temperature ($T_m$), relaxation time ($\tau_{\varepsilon'}$ and $\tau_m$), and highest dielectric constant ($\varepsilon$). The ion transport parameters, i.e., ion mobility ($\mu$) and diffusion coefficient ($D$) are also in good agreement with electrical conductivity value. The high value of ion transference number (~ 100%) and broad voltage stability window (~ 5 V) of the intercalated polymer nanocomposite suggest their suitability for energy storage/conversion devices.

## Experimental section

### Materials

Polymers polyethylene oxide (PEO; $1 \times 10^6$ g/mol) and polyvinyl chloride (PVC; $6 \times 10^4$ g/mol) were procured from the Sigma-Aldrich. Lithium hexafluorophosphate ($LiPF_6$) was chosen as salt purchased from Sigma-Aldrich. Tetrahydrofuran (THF) was used as solvent purchased from Sigma-Aldrich and was used as received. The Na-montmorillonite clay (Na-MMT; SWy–2) has been procured from the clay minerals society (USA) and added in different weight fraction relative to polymer host. Montmorillonite is a 2:1 layered hydrated aluminosilicate, with a triple-sheet sandwich structure (clay platelet) consisting of a central, hydrous alumina octahedral sheet (O-layer), bonded to two silica tetrahedral sheets (T-layer) by shared oxygen ions. The unit cell of this ideal structure has a composition $[Al_2(OH)_2(Si_2O_5)_2]_2$.

According to the manufacturer, the MMT product had a cation exchange capacity (sum of the exchangeable cations) of 80 mequiv/100 g, interlayer charge ~ 0.55, and specific surface area ~ 31.82 $m^2$/g. The nanoclay was modified with dodecylamine (DDA) before use and is termed as MMMT clay throughout the manuscript.

### Clay modification

In view of preparation of intercalated polymer nanocomposite films, the nature of clay needs to be organophilic; therefore, organic modification is utmost necessary before its use in polymer salt complex. The procured sodium montmorillonite has been modified using dodecylamine as a surfactant by an ion exchange reaction. In

this process, $Na^+$ ions (the natural occupancy of clay channels) located in between clay platelets are replaced by dodecyl ammonium ion and hence the MMT changes from hydrophilic to organophilic. The clay platelets are coated with charged molecules, and it results in separation of clay platelets owing to repulsion force (in c-direction) [27]. Figure 1 a shows the clay modification.

## Preparation of polymer nanocomposites

The polymer nanocomposites were prepared using solution cast technique. Firstly, the appropriate amount of PEO (1 g) and PVC (1 g) were dissolved separately in the THF (10 ml) solvent and stirred continuously till a homogenous and transparent solution is obtained. Then, the stoichiometric ratio (O/Li = 8) of $LiPF_6$ was added in the blend polymer solution and stirred again till the homogenous solution is obtained. After that, the pre-sonicated MMMT in various weight ratios was added in the blend polymer salt matrix and the same was stirred for 24 h to achieve uniform mixing of the nanoclay. The prepared solutions were cast on the

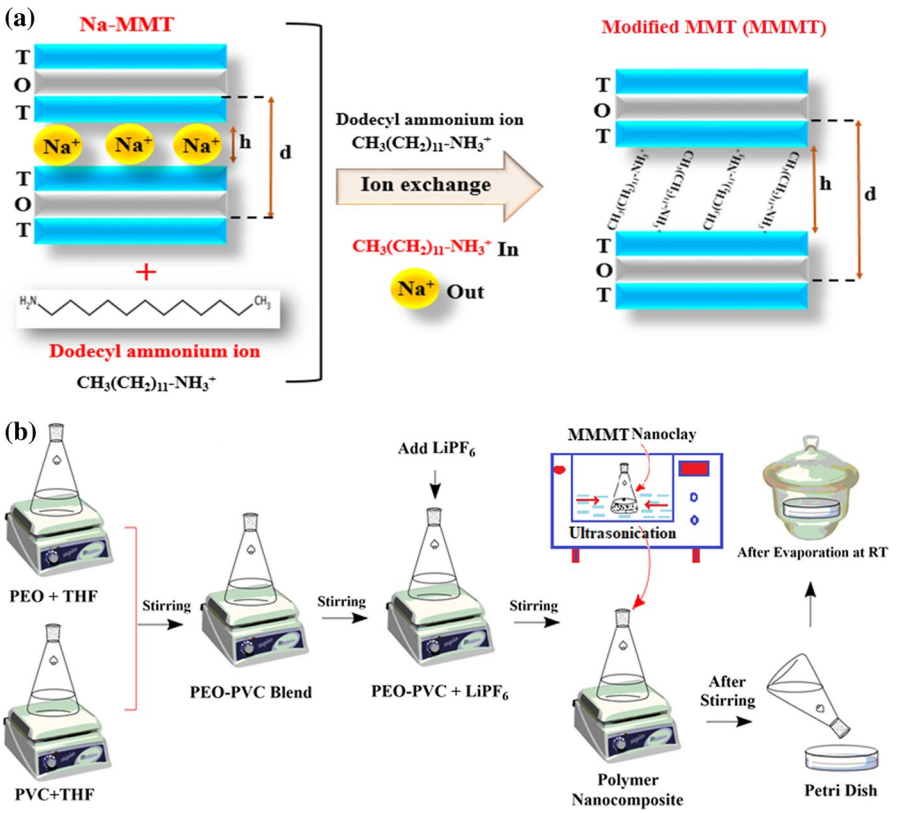


**Fig. 1** **a** Modification of nanoclay, where *h* is the interlayer distance, and *d* is the basal spacing, and **b** schematic representation of solution cast technique

Petri dishes and kept at room temperature for slow evaporation of the solvent, followed by vacuum drying at 50 °C for 24 h. Then, the films are peeled off from the Petri dishes, and free-standing film is kept in the desiccator (with silica gel) again for further characterization. The solution cast technique is shown in Fig. 1b in detail. The thickness of the film was in the range of 100–130 μm measured by Digital micrometer screw gauge (Mitutoyo Digimatic Micrometer). The prepared polymer nanocomposite films are [(PEO–PVC) + $LiPF_6$ (O/Li = 8) + $x$ (MMMT), $x$ = 0, 1, 3, 5, 7, 10, 15, 20 wt%]. The blend polymer (PEO–PVC) is denoted by pure, (PEO–PVC) + $LiPF_6$ (O/Li = 8) by 0% MMMT, and for nanoclay concentration $x$% (MMMT), where $x$ = 1, 3, 5, 7, 10, 15, 20.

## Characterizations

X-ray diffraction analysis was performed (Model: Bruker D8 Advance with Cu-filtered) with Cu-$K_\alpha$ radiation ($\lambda$ = 1.54 Å) at room temperature in the Braggs angle range ($2\theta$) from 2° to 60° with scan 0.01 degree per minute. Field emission scanning electron microscopy (FESEM) was used to study the surface morphology (FESEM: Carl Zeiss product) and taken in a high vacuum after sputtering the samples with gold in order to prepare conductive surfaces. The transmission electron microscopy (TEM) images are obtained at 100 kV. The Fourier transform infrared spectra of the samples were recorded in the range of 400–3000 $cm^{-1}$ Bruker Tensor 27, Model: NEXUS–870 to confirm the complex formation at a scan rate of 4 $cm^{-1}$.

The electrical conductivity has been measured using an electrochemical analyzer (CHI 760; USA) in the frequency range 1 Hz–1 MHz and broad temperature range (40–100 °C, @ 10 °C). The PNC film is sandwiched between the two stainless (SS) blocking electrodes, and an ac signal (~ 20 mV) is applied across the cell. The thermal activation energy for ionic transport is estimated from the slope of the linear fit of the Arrhenius plot. The linear variation in log ($\sigma$/S $cm^{-1}$) versus 1000/$T$ plot suggests a thermally activated process represented by $\sigma = \sigma_o \exp\left(-E_a/kT\right)$, where $\sigma_o$ is the constant pre-exponential factor and $E_a$ is the activation energy. The parameter $T$ stands for the absolute temperature and $k$ for the Boltzmann constant. Differential scanning calorimetry (DSC) has been performed, in a temperature range of − 90–100 °C (@10 °C per minute in Ar/N2 atmosphere) using DSC-3500 Sirius (NETZSCH). Thermo gravimetric analyzer (TGA; SHIMADZU–DTG-60) has been performed in a temperature range of 30 °C–600 °C (@10 °C) per minute in nitrogen atmosphere). The voltage stability window is obtained using the linear sweep voltammetry (LSV) technique using the cell configuration SS|PNC|SS in the voltage range − 3 to + 3 V. The ion transference ($t_{ion}$) number was measured using $i$–$t$ characteristics by applying a dc voltage of 0.02 V across cell SS|PNC|SS. The impedance data are transformed into the dielectric constant ($\varepsilon'$), dielectric loss ($\varepsilon''$), and complex conductivity ($\sigma'$ and $\sigma''$). All plots are fitted with corresponding equations by Origin® 8 software to evaluate the various parameters that enable us to explore the ion dynamics.

## Results and discussion

### X-ray diffraction analysis

Figure 2 shows the XRD pattern of the prepared PNCs films at room temperature in two broad regions, i.e., at a high angle ($10° \leq 2\theta \leq 60°$), and at a low angle ($2° \leq 2\theta \leq 10°$). The characteristics peaks of the PEO are located at $2\theta = 19.23°$ (associated with 120 planes) and 23.78° (associated with 032, 112 planes), owing to the crystalline nature of polymer matrix (Fig. 2a). The minor peaks present near 33° and 37° are associated with pure PEO. Addition of salt changes the peak position of PEO, and the absence of any salt peak in the plot confirms the complete salt dissociation [28]. Addition of salt also influences the PEO minor peaks, and reduction in intensity infers the enhancement of the amorphous content. The change in the peak position and shape further with the addition of nanoclay indicates the reduction in crystallinity as evidenced in terms of decreasing peak intensity. It provides sufficient evidence of the composite formation and enhancement of the amorphous content. The alteration of peak position and intensity change provides strong evidence of the sufficient interaction between the polymer matrix and nanoclay. To get insights into the further evidence of the role of nanoclay in the polymer matrix, modified MMT characteristic peak (001) was analyzed in detail (Fig. 2b) via low angle X-ray diffraction pattern. It is seen that just after doping of low clay content, the (001) peak shifted toward lower diffraction angle side and the *d*-spacing (clay

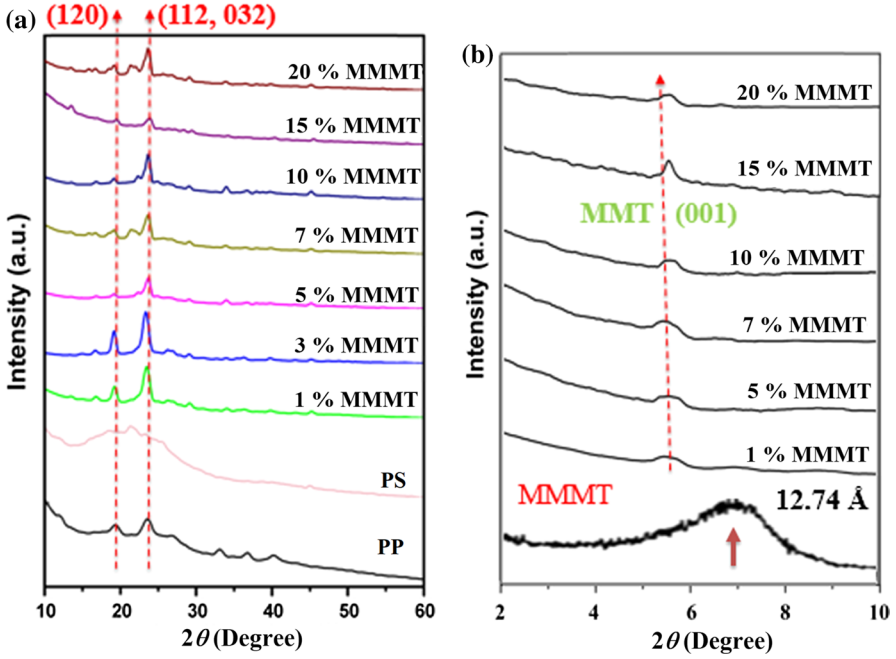


**Fig. 2** XRD pattern of PNC films PP (Pure blend), PS (Polymer salt), PEO–PVC + $LiPF_6$ + *x* wt% MMMT in the range of diffraction angle; **a** $10° \leq 2\theta \leq 60°$, and **b** $2° \leq 2\theta \leq 10°$

**Table 1** Values of 2$\theta$ (degree), $d$-spacing (Å) and $R$ (Å) of polymer nanocomposites films [(PEO–PVC)–$LIPF_6$ + $x$ wt% MMMT]

| Sample | (120) Reflection peak parameters | | | (112)/(032) Reflection peak parameters | | |
|---|---|---|---|---|---|---|
| | 2$\theta$ (degree) | $d$-Spacing (Å) | $R$ (Å) | 2$\theta$ (degree) | $d$-Spacing (Å) | $R$ (Å) |
| Pure blend | 19.23 | 4.61 | 5.76 | 23.78 | 3.78 | 4.72 |
| 0% | 18.45 | 4.80 | 6.00 | 23.18 | 3.83 | 4.78 |
| 1% | 19.24 | 4.61 | 5.76 | 23.46 | 3.79 | 4.73 |
| 3% | 19.14 | 4.63 | 5.79 | 23.32 | 3.81 | 4.76 |
| 5% | 19.11 | 4.66 | 5.83 | 23.10 | 3.85 | 4.81 |
| 7% | 19.11 | 4.66 | 5.83 | 23.62 | 3.77 | 4.71 |
| 10% | 19.14 | 4.63 | 5.79 | 23.61 | 3.77 | 4.71 |
| 15% | 19.46 | 4.55 | 5.69 | 23.81 | 3.73 | 4.66 |
| 20% | 19.16 | 4.63 | 5.79 | 23.68 | 3.75 | 4.69 |

**Table 2** XRD data of 001 peak of MMT in PNCs

| Sample | 2$\theta$ (degree) | $d$-Spacing (Å) | Gallery width (Å) |
|---|---|---|---|
| Pristine MMT [30] | 7.1 | 12.71 | 3.11 |
| PEO–PVC + $LiPF_6$ + $x$ wt% MMMT | | | |
| 1 | 5.5 | 16.04 | 6.44 |
| 3 | 5.6 | 16.04 | 6.44 |
| 5 | 5.4 | 16.38 | 6.78 |
| 7 | 5.7 | 15.71 | 6.11 |
| 10 | 5.5 | 16.38 | 6.78 |
| 15 | 5.5 | 16.38 | 6.78 |
| 20 | 5.6 | 15.71 | 6.11 |

gallery with) increases accordingly. To confirm the polymer intercalation and clear interaction with polymer chain, $d$-spacing ($d = n\lambda/\sin\theta$) and inter-chain separation ($R = 5\lambda/8\sin\theta$) is analyzed properly [29]. The obtained parameters are summarized in Table 1. It may be noticed that both parameters increase with the addition of nanoclay up to optimum content with the addition of nanoclay. It is attributed to the complex formation and the presence of sufficient interaction between the polymer–salt and nanoclay.

The polymer intercalation inside the clay galleries is analyzed in detail by investigating the changes in the characteristics peak of the clay (associated with 001 planes) [30]. XRD results indicate noticeable changes in the $d_{001}$ peak of clay as compared to pristine clay (Fig. 2b). The shifting of peak toward the lower angle side indicates an increase in the clay gallery width which infers the cation-coordinated polymer chain intercalation inside the clay galleries (Table 2). It may be concluded that the XRD spectra evidence the polymer intercalation. The polymer intercalation is further confirmed by the TEM and FTIR analysis.

### Field emission scanning electron microscopy analysis

Figure 3 depicts the FESEM micrographs of the pure PEO (Fig. 3a), PEO–PVC blend (Fig. 3b), polymer salt matrix (Fig. 3c), and polymer salt matrix with 5 wt% MMMT (Fig. 3d). It may be observed that change in morphology of the PEO–PVC blend polymer as compared to pure PEO indicates the disruption of the semicrystalline nature of PEO and confirms the blend formation. The transition from the rough surface morphology to smooth morphology suggests the enhancement of the amorphous content. Further, addition of salt in the blend matrix changes the morphology which suggests the complex formation due to the interaction between cation and ether group of PEO (O–$Li^+$). Addition of nanoclay in the polymer salt matrix indicates the sufficient interaction in between the clay platelets and the polymer matrix. The EDS spectra confirm the presence of the clay in PNCs (Fig. 3e). Figure 3f shows the elemental mapping of the different elements of the nanoclay and supports the EDS spectrum. Further evidence of the polymer intercalation is done by TEM analysis.

### Transmission electron microscopy analysis

The morphology of the PNCs was further investigated by acquiring the transmission electron microscope (TEM) images for polymer salt and polymer salt matrix + 5% MMMT (Fig. 4). While the morphology of the intercalated PNCs shows noticeable changes as compared to the pristine polymer salt matrix. The dark strips depict the clay platelets (shown by arrows) which implies the polymer intercalation, and gray/white area is polymer salt matrix. The light strips in the image are exfoliated clay. The presence of clay platelets in the PNCs is in perfect agreement with the XRD results. The structural and morphological analysis evidenced the effective role of nanoclay (polymer intercalation) [31, 32].

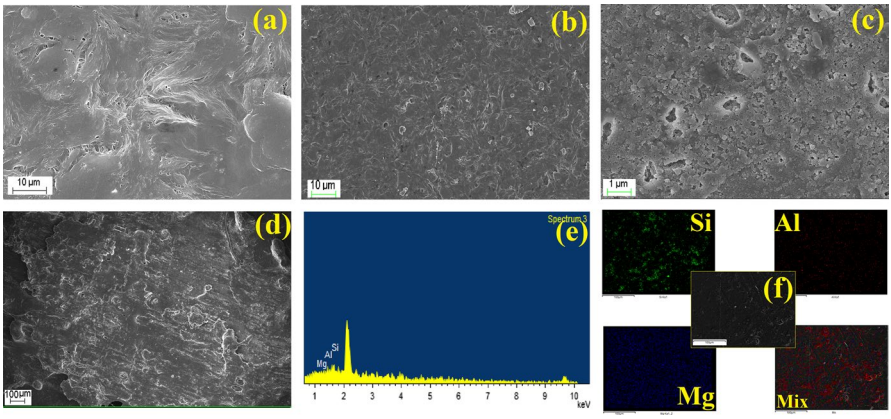


**Fig. 3** Surface morphology of **a** Pure PEO, **b** PEO–PVC blend, **c** polymer salt complex, **d** polymer salt complex + 5% MMMT, **e** EDS spectrum of PNC with 5% MMMT, and **f** elemental mapping of Si, Al, Mg in the intercalated PNC

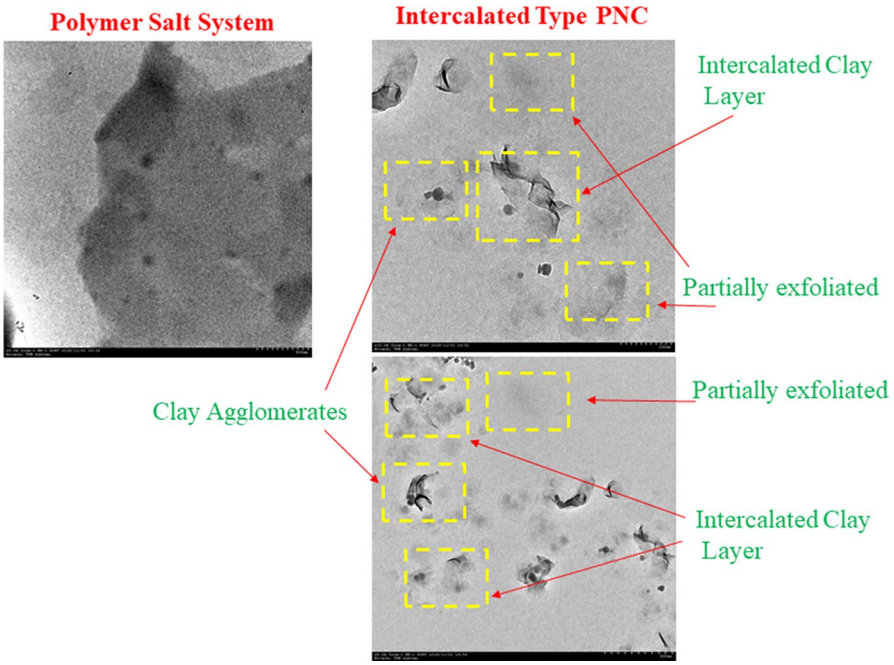


**Fig. 4** TEM images of the clay-free and polymer-intercalated (5 wt% MMMT) PNCs

## Fourier infrared (FTIR) spectroscopy analysis

FTIR spectra have been recorded in the absorbance mode at room temperature in the wavenumber region 400–3000 $cm^{-1}$ (Fig. 5). The vibrational bands of pure PEO are obtained at 843 $cm^{-1}$ ($CH_2$ asymmetric rocking), 960 $cm^{-1}$ ($CH_2$ symmetric rocking), 1060–1150 $cm^{-1}$ (C–O–C stretching triplet), 1240–1297 $cm^{-1}$ ($CH_2$ twisting), 1343–1366 $cm^{-1}$ ($CH_2$ wagging doublet), 1466 $cm^{-1}$ ($CH_2$ scissoring), and 2886 $cm^{-1}$ ($CH_2$ stretching) [33]. The vibrational band of the PVC are obtained at, 613 $cm^{-1}$ ($\nu$ (C–Cl)), 636 $cm^{-1}$ ($\nu$ (C–Cl)), 689 $cm^{-1}$ ($\nu$ (C–Cl)), 961 $cm^{-1}$ ($r$ ($CH_2$)), 1095 $cm^{-1}$ ($\nu$ (C–C)), 1255 $cm^{-1}$ ($\delta$ (C–H of CHCl)), 1330 $cm^{-1}$ ($\delta$ (C–H of CHCl)), 1429 $cm^{-1}$ ($w$ ($CH_2$)), 2909 $cm^{-1}$ ($\nu$ (C–H of $CH_2$)), and 2968 $cm^{-1}$ ($\nu$ (C–H CHCl)) [34]. A broad absorption band is observed in the wavenumber region 750–1350 $cm^{-1}$ and corresponds to the four Si–O stretching modes of the MMT (three in-plane mode (1120; 1048; and 1025 $cm^{-1}$), and one out-of-plane mode (1080 $cm^{-1}$) [35]. The FTIR spectrum in the wavenumber region 600–3000 $cm^{-1}$ is shown in Fig. 5. In order to explain the obtained data, the discussion has been explained in light of microscopic interaction among the polymer, ion, and clay interaction.

The FTIR spectra of the blend PEO–PVC is shown in Fig. 6i–iii in different wavenumber range. It is important to note that after blend formation, characteristics peak of the PEO and PVC shows a shift in peak position and change in intensity. The peak located at 1100 $cm^{-1}$ associated with C–O–C stretching mode shifts to

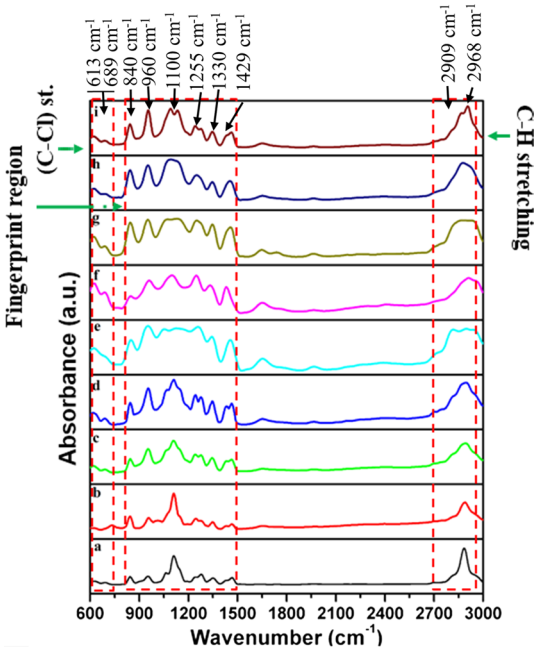


**Fig. 5** FTIR spectra for a. Pure PEO–PVC, and $x$% MMMT, $x$ = b. 0, c. 1, d. 3, e. 5, f. 7, g. 10, h. 15 and i. 20

1111 $cm^{-1}$ and peak of trans (C–H) wagging mode located at 961 $cm^{-1}$ in PVC shifts to 951 $cm^{-1}$ in PEO–PVC blend. The peak located at 1255 $cm^{-1}$ associated with (C–H) rocking, 1330 $cm^{-1}$ associated with $CH_2$ deformation mode in PVC shifts to 1241 $cm^{-1}$ and 1349 $cm^{-1}$, respectively. The $CH_2$ wagging mode of PVC observed at 1429 $cm^{-1}$ shows a small shift toward lower wavenumber side. These changes evidence the presence of strong interaction between PEO and PVC matrix of blended PEO–PVC. It may be noted that the presence of characteristics peaks of individual polymer infers the miscibility of polymer skeleton and is attributed to the, (1) intermolecular hydrogen bonding, and (2) van der Walls interaction between the PEO and PVC polymer chain [36]. The above analysis established the PEO–PVC blend formation.

## Polymer–ion interaction

To explore the polymer–salt interactions, firstly the characteristic vibration modes of salt and polymer are studied. The fundamental peak of the $LiPF_6$ is located at 837 $cm^{-1}$ ($\nu(PF_6^-)$, and 1164 $cm^{-1}$ ($\nu(PF_5)$ [37]. The characteristics peak of the PEO–PVC located at 843, 951, 1063, 1111, 1241, 1277, 1349, 1427, 1466, and 2883 $cm^{-1}$ is shifted to 842, 956, 1014, 1119, 1244, 1273, 1347, 1429, 1464, and 2887 $cm^{-1}$ on addition of salt. This provides strong evidence of the complexation between PEO–PVC and $LiPF_6$. The electron-rich group of the polymer is the most favorable site for cation coordination. Now, to investigate the actual cation ($Li^+$) coordination out of two available sites, (1) ether group (–O–) of PEO and (2) –Cl of PVC, the FTIR spectra are studied in detail.

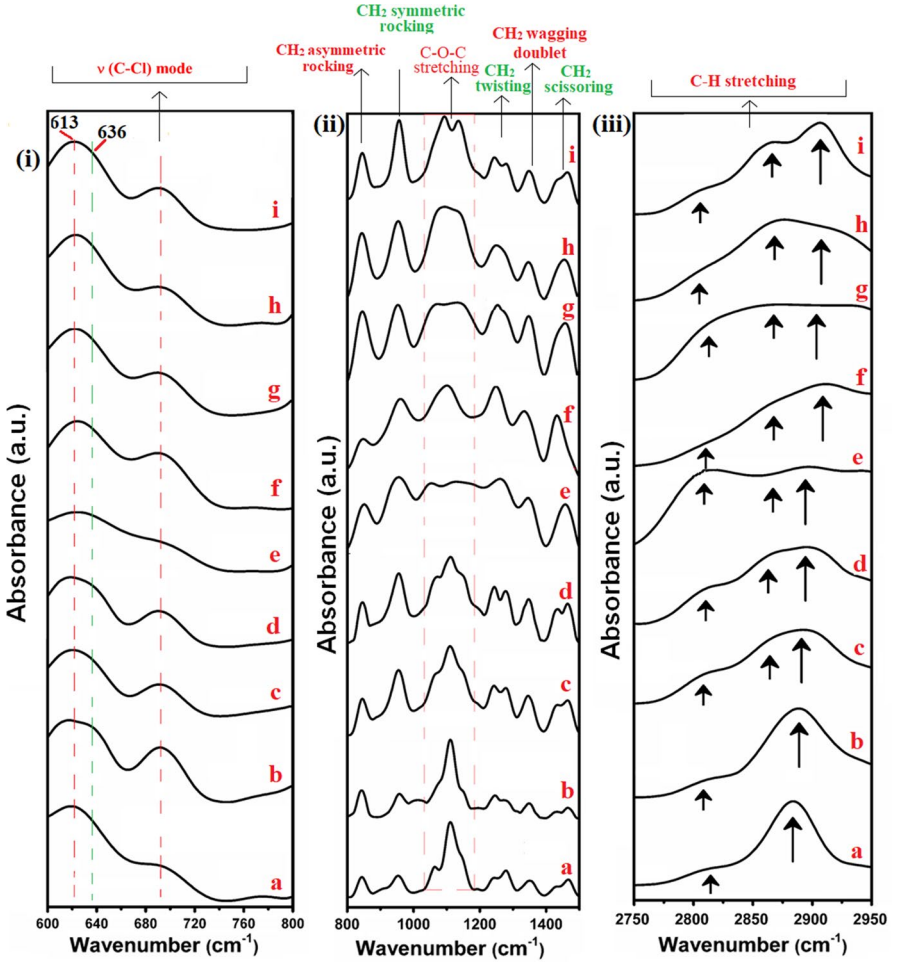


**Fig. 6** FTIR spectra in the wavenumber region, (i) 600–800 $cm^{-1}$, (ii) 800–1500 $cm^{-1}$, (iii) 2750–2950 $cm^{-1}$ for the PNCs films a. Pure PEO–PVC, and *x*% MMMT, *x* = b. 0, c. 1, d. 3, e. 5, f. 7, g. 10, h. 15 and i. 20

Figure 6i shows the absorbance spectra in the wavenumber 600–800 $cm^{-1}$ and corresponds to 613 $cm^{-1}$ ($\nu$ (C–Cl)), 636 $cm^{-1}$ ($\nu$ (C–Cl)), 689 $cm^{-1}$ ($\nu$ (C–Cl)) of PVC. It may be noted that all the peaks are almost identical in terms of its shape and intensity on the addition of salt in the blend matrix. This identical nature of peak position confirms that the $Li^+$ coordination has zero probability with –Cl group of PVC and reveals the absence of any interaction of cation with the polar group of PVC. Now, to augment the cation coordination with the ether group of PEO, the FTIR spectra are studied as shown in Fig. 6ii. As the characteristics peak of PEO (–C–O–C– stretching) is located near 1100 $cm^{-1}$ and is associated with the amorphous content of PEO. The frequency of this peak is sensitive to the interaction of the electron-rich ether group and cation [38]. The addition of salt alters peak

position and intensity. This indicates that PEO seems to be more favorable for cation coordination and is an actual site in the blend polymer matrix [39]. The changing profile of the C–O–C band of PEO and unaltered profile of C–Cl in PVC suggests the cation coordination with electron-rich ether group of PEO. The crystalline phase shoulder peak of the PEO at 1144 $cm^{-1}$ is suppressed, while peak near 1056 $cm^{-1}$ gradually disappeared on the addition of salt [40]. The above changes in the characteristics peak of PEO provide strong evidence of ion–dipolar coordination between the electron-rich ether group of PEO and cation, which infers the reduction in PEO crystalline phase. So, on the basis of the above evidence, it may be concluded that the cation coordination occurs with an ether group of PEO and polymer reorganization tendency is reduced; hence, enhanced amorphous content is obtained.

#### Polymer–nanoclay interaction

The effect of nanoclay addition on the vibrational modes of the polymer matrix is shown in the wavenumber region 800–1500 $cm^{-1}$ (Fig. 6ii, a–i). It may be noted that the addition of clay influenced the peak position and shape of the characteristics band of the blend. The band located at 960 $cm^{-1}$ associated with $CH_2$ symmetric rocking of PEO indicates the increase in peak intensity and changes in peak profile. The shift in peak is observed even after the addition of a small amount of MMMT. The fundamental peak of PEO located at 1100 $cm^{-1}$ is associated with C–O–C stretching mode and after even a small amount of nanoclay, a shoulder appears, and with the addition of clay, peak get split into two peaks. It may be noted that with an increase in clay content, the shoulder at 1144 $cm^{-1}$ disappears and for 5 wt% MMMT, the only a single peak is observed which infers the crystalline phase of PEO (Fig. 6ii, e). Along with this, another shoulder at the lower wavenumber side (~ 1056 $cm^{-1}$) disappears with clay addition and indicates the disruption of the crystalline phase [40]. It suggests that the nanoclay is effective in altering the polymer chain arrangement by confining within its clay galleries, and increased interlayer spacing accommodates more polymer chains with cation. At high nanoclay content, a clear signature of two peaks is observed.

Peak located at 1240–1297 $cm^{-1}$ associated with $CH_2$ twisting mode shows splitting after addition of clay in the polymer salt matrix and, $CH_2$ wagging doublet at 1343–1366 $cm^{-1}$ also shows very little shift in wavenumber. The $CH_2$ scissoring mode located at 1466 $cm^{-1}$ shows peak broadening and a shift in peak position confirms the strong possibility of polymer–clay interaction in PNC films. The $CH_2$ stretching mode located at 2886 $cm^{-1}$ indicates the remarkable peak broadening, and reduction in peak intensity are observed after clay addition (Fig. 6iii, a–i). The C–H stretching mode of near 2900 $cm^{-1}$ provides strong evidence of polymer–clay interaction. These changes in peak profile (broadening and change in intensity) and a shift in position confirm the effective role played by nanoclay on the polymer salt matrix, hence the presence of polymer–nanoclay interactions. It is believed that the polymer intercalation disrupts the polymer reorganization tendency, and formation of the amorphous phase is beneficial for ion transport. This provides strong evidence of the $–Li^+–O–$ coordination, and change in peak profile of vibrational bonds confirms the formation of PNCs.

### Ion–ion interaction

The $PF_6^-$ anion mode near 840 $cm^{-1}$ is important to examine carefully to observe the cation–anion interaction. It is well-known that the cations are insensitive, whereas anions are sensitive to FTIR; therefore, the information of ion–ion interaction has been derived from the absorbance mode of $PF_6^-$ and is sensitive to anion environment which reflects the salt dissociation. The peak area provides quantitative information about ionic species distribution in PNCs. The uncoordinated or free $PF_6^-$ anion possesses octahedral ($O_h$) symmetry and bond angle formed by F–P–F is found to be exactly 90°. There are a total of 15 vibrational fundamental modes of free anion and can be represented as $\Gamma = a_{1g} + e_g + t_{1g} + t_{2g} + 3t_{1u} + t_{2u}$, where $\vartheta_1(a_{1g}), \vartheta_2(e_g)$, and $\vartheta_5(a_{2g})$ modes are Raman active; the $\vartheta_3(t_{1u})$and $\vartheta_4(t_{1u})$ modes are IR active; and $t_{1g}$ and $t_{2u}$ modes are silent in both Raman and IR spectra [41]. The vibrational energy of the free anion is $\vartheta_1 = 741(R), \vartheta_2 = 567(R), \vartheta_3 = 838(\mathrm{IR}), \vartheta_4 = 558(\mathrm{IR})$, and $\vartheta_5 = 470(R)$ $cm^{-1}$. In the FTIR spectra, it is noticed that the strongest IR-active free anion peak at 838 $cm^{-1}$ depicts some asymmetry due to ion–ion interactions (between neighboring ion or ion aggregation), and this alteration results in peak splitting. This indicates the lowering of free anion symmetry from octahedral to the tridentate ion ($O_h \rightarrow C_{3\vartheta}$) [42]. We are interested in the $\vartheta_3 = 838(\mathrm{IR})$ mode and is deconvoluted to probe the fraction of free anions ($-PF_6^-$) and ion pairs ($Li^+$–$PF_6^-$) using PeakFit (v4) software as both bands are IR active.

Figure 7 depicts the spectral pattern of $PF_6^-$ anion in the wavenumber region of 820–870 $cm^{-1}$. The bird-eye-view of the anion vibration mode indicates the presence of asymmetry and is originated from the anion interactions with counter anion or ion aggregation. To understand the clay role in dissociating salt, the absorbance was deconvoluted into two bands using PeakFit (V 4.02) software with Voigt Amp profile, and two bands are observed by decomposing the anion band. The band located at lower wavenumber side corresponds to free $PF_6^-$(does not interact directly with a cation), and another band at high wavenumber is that of bound or ion pairs ($Li^+$–$PF_6^-$). The fraction of free anions (FFA) and a fraction of ion pairs (FIP) is obtained using Eq. 1, and the best fit is said to be measured by the correlation coefficient ($r^2$).

$$\mathrm{FFA} = \frac{\text{Area of free ion peak}}{\text{Total peak area}} \text{ and } \mathrm{FIP} = \frac{\text{Area of ion pair peak}}{\text{Total peak area}} \tag{1}$$

Figure 7i shows the plot of FFA and FIP against nanoclay content. It shows that the fraction of free anions increase with the addition of MMMT content. It is clearly seen that even at low clay content, there is a small increase and is the highest for the 5 wt% MMMT. At, this nanoclay content sufficient interaction occurs between polymer, cation, and nanoclay assist the PNC matrix to dissolve more salt. The combined effect of the negative surface charge layer and a polar group of PEO results in better salt dissociation and infers the increased number of free charge carriers [43]. However, when the clay content exceeds the 5 wt%, the fraction of free anions decreases and is attributed to the reduction in surface area owing to nanoclay

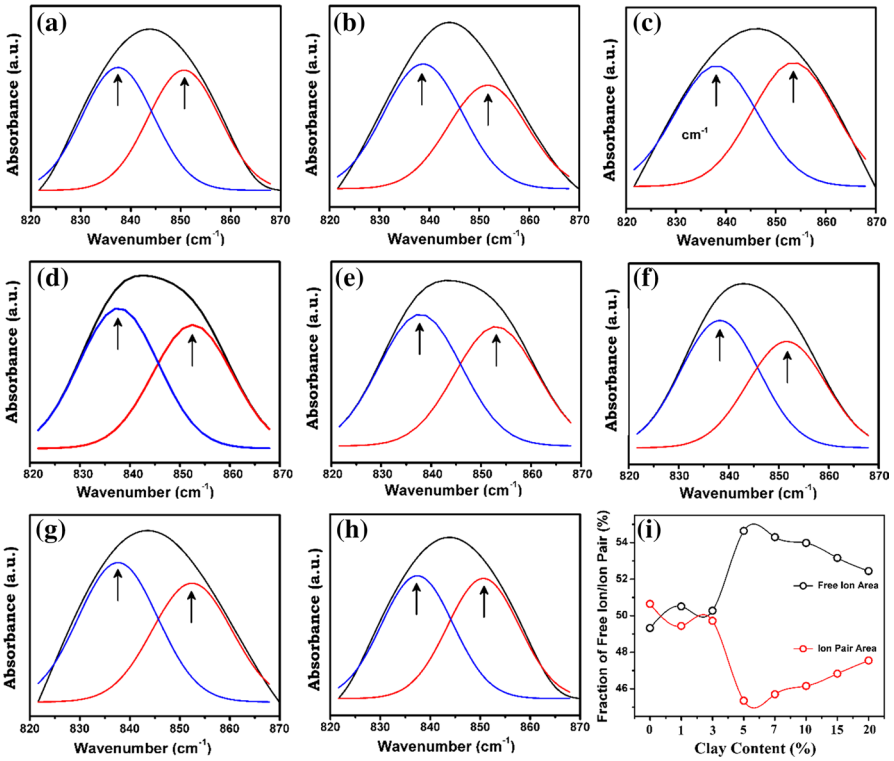


**Fig. 7** Deconvolution bands of $PF_6^-$ mode for polymer nanocomposites with $x$ % MMMT, $x$ = **a** 0, **b** 1, **c** 3, **d** 5, **e** 7, **f** 10, **g** 15, **h** 20, and **i** variation of the fraction of free anion and ion pair for different clay content

aggregation. Therefore, at high content, nanoclay is not effective in dissociating the salt and an associated maximum in a fraction of ion pairs is observed.

### The probe of clay intercalation through Si–O mode of nanoclay

FTIR spectroscopy is again very sensitive to prove the intercalation/exfoliation of nanoclay in intercalated PNC system as suggested by Cole [35]. A broad absorption band is observed in the wavenumber region 750–1350 $cm^{-1}$ and corresponds to the four Si–O stretching modes of the MMT (three in-plane mode (1120; 1048; and 1025 $cm^{-1}$), and one out-of-plane mode (1080 $cm^{-1}$) [35]. It suggests that the position and peak shape of out-of-plane mode located at 1080 $cm^{-1}$ is highly sensitive to the physical state of nanoclay or interlayer gallery width. In the present study, the Si–O–Si band was explored by deconvoluting it in four peaks located at: peak I (~ 1024 $cm^{-1}$), peak II (~ 1045 $cm^{-1}$), peak III (~ 1080 $cm^{-1}$; out-of-plane mode), and peak IV (~ 1115 $cm^{-1}$). From Fig. 8, all the peaks display a change in profile and peak III is more sensitive and may be considered an

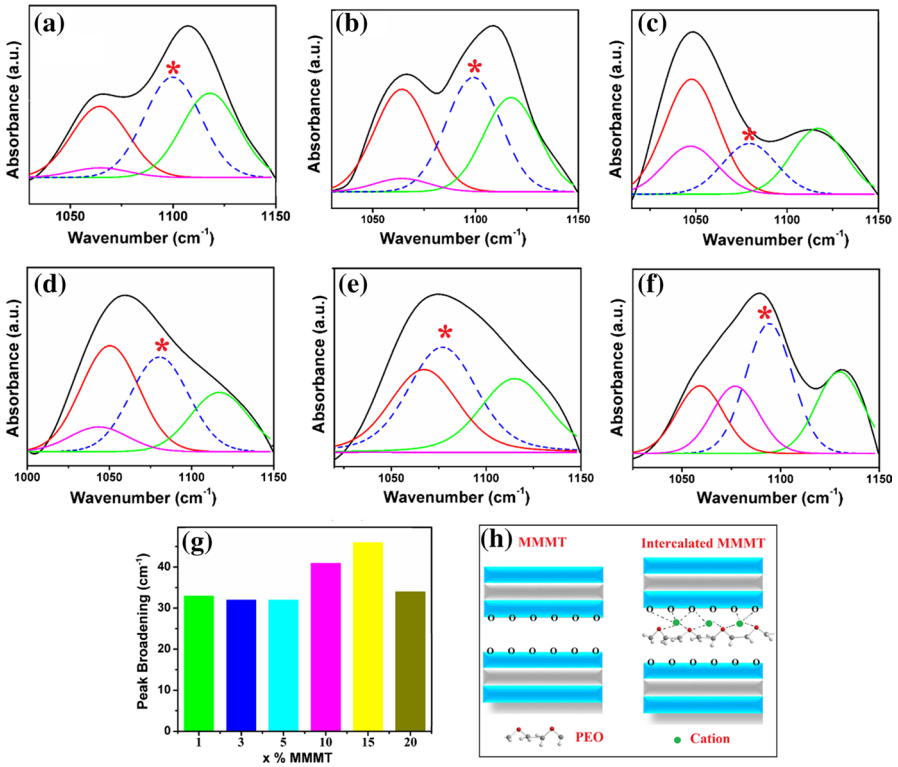


**Fig. 8** FTIR spectra of Si–O vibration mode (out-of-plane) of MMMT in PNCs films, *x*% MMMT, *x* = **a** 1, **b** 3, **c** 5, **d** 10, **e** 15, **f** 20, **g** variation of peak broadening, and **h** schematic diagram of intercalation

indicator of intercalation (shown by the dotted blue line and indicated by *) of nanoclay during insertion of cation-coordinated polymer into it.

It is important to note that the peak becomes narrow with diminished intensity. The above-said changes suggest that the polymer chain gets confined inside clay galleries that enhance the interlayer spacing and confirmed by the effect on Si–O mode. Same has been reported in other polymers also [35]. This also suggests the possibility of cation coordination with a surface charge of clay, and it will provide addition conducting sites for cation that will be reflected in the conductivity studies as discussed below.

It may be concluded from the details investigation of FTIR studies, (1) polymer, salt, and nanoclay play effective role in PNC matrix, (2) blend formation and cation coordination with ether group of PEO are confirmed (3) polymer intercalation is confirmed from Si–O mode of MMMT, and (4) fraction of free anions increases with MMMT content. Above-said FTIR results will be helpful in explaining the enhancement of ionic conductivity, transport parameters, flexibility, and voltage stability window with the addition of nanoclay. The clay galleries

of nanoclay will provide accommodation to polymer chain with cation and will support the faster cation migration by minimizing the concentration polarization.

## Electrochemical analysis

### Impedance spectroscopy

The impedance spectra of the prepared PNCs with different clay contents are shown in Fig. 9a, at 40 °C. The log–log presentation of impedance plots is displayed for a better comparison of different PNCs systems. The detailed eagerness of this representation over the traditional plot is mentioned in our previous study and somewhere else by Jonscher [44].

Figure 9a shows the plot of the imaginary part of impedance against a real party for various PNCs films. It may be noted that all systems show two arcs, one lying on the high-frequency side followed by another at the lower-frequency side. The dip observed in the plot corresponds to the bulk resistance of PNC film and corresponds

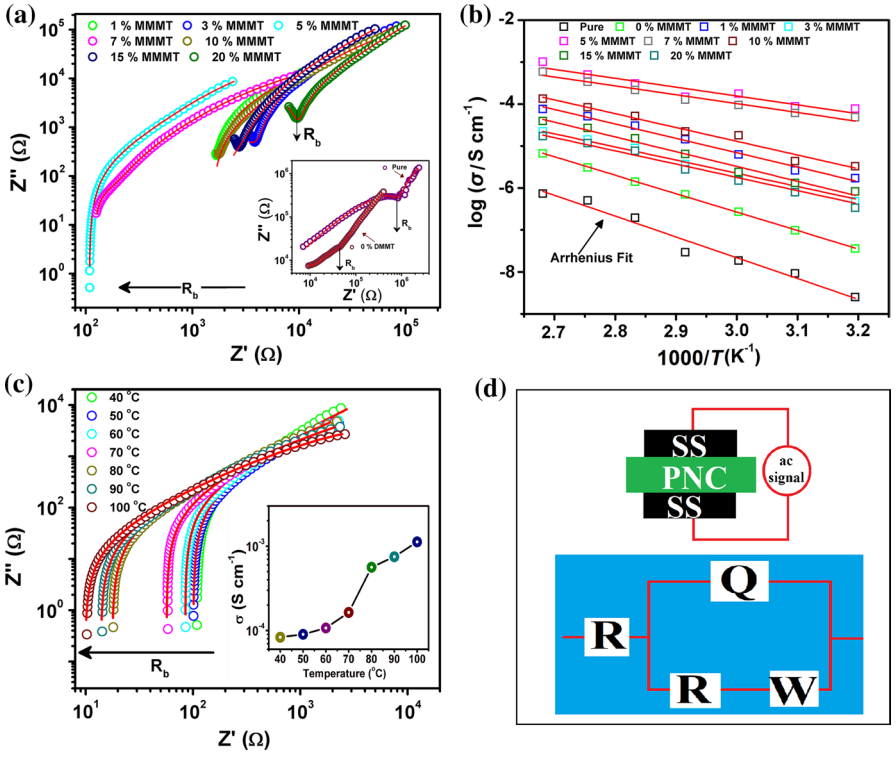


**Fig. 9** **a** Room temperature log–log complex impedance plots for different PNCs films. The inset depicts cell configuration and equivalent circuit, **b** Impedance plot for 5 wt% MMMT in temperature (40–100 °C) range. Inset of b depicts conductivity variation with temperature, **c** Arrhenius plot, and **d** cell assembly and equivalent circuit. The solid red line is the fitted plot in Figure **a**–**c**

to the minima in the imaginary axis. For the pure polymer, the length of the high-frequency arc is large and reduces with the addition of salt (Inset). The high-frequency arc is associated with the bulk properties of the PNC film, i.e., ion migrations via ions, while the low-frequency arc imitates the double-layer capacitance at the electrode–electrolyte interface. It implies the absence of electronic conductivity, which is desirable for faster ion transportation [38, 45]. The experimental impedance was fitted with software ($Z_{SimpWin}$), and an electrical equivalent circuit (EEC) was fitted (Fig. 9d). It may be noted that fitted data (shown by a solid line) aggress well with the experimental data. The EEC comprise of a resistance in series with a parallel combination of constant phase element and another resistance in series with a Warburg impedance. It may be noted that the value of bulk resistance decreases with the addition of clay and is attributed to an effective change in the polymer chain arrangement that promotes the faster ion conduction [46]. With the addition of even a small amount of clay decrease in the high-frequency arc is observed and with further clay addition, the only low-frequency arc is visible that indicates the better salt dissociation and formation of the double layer.

### Electrical conductivity analysis

The electrical conductivity has been calculated using the $R_b$ obtained from the minima of the imaginary part in the log–log plot which is used subsequently for the evaluation of electrical conductivity. The electrical conductivity is shown in Table 3. It may be noted that the addition of even a small amount of clay increases the electrical conductivity and increases with further addition. The highest conductivity is obtained for the 5% MMMT clay content and is about $8.15\times10^{-5}$ S cm$^{-1}$. The optimum conducting composition (OCC) is 5 wt% MMMT for the present investigation and reflects the balanced attractive forces between polymer–cation–nanoclay layers which help in the release of the cation. It is also linked with the proper dispersion of nanoclay that enhances the dielectric properties of nanoclay. This results in the

**Table 3** Different contributions of electrical conductivity, transference number, activation energy, and voltage stability window for (PEO–PVC)–$LIPF_6$ + $x$ wt% MMMT

| Sample name | Transference number | | Conductivity (S cm$^{-1}$) | | | $E_a$ (eV) | ESW (V) |
|---|---|---|---|---|---|---|---|
| | $t_{ion}$ | $t_{ele}$ | Electrical | Ionic | Electronic | | |
| Pure | – | – | $3.33\times10^{-8}$ | – | – | 0.98 | 3.12 |
| 0% | 0.93 | 0.07 | $1.64\times10^{-7}$ | $1.52\times10^{-7}$ | $1.14\times10^{-8}$ | 0.87 | 3.48 |
| 1% | 0.94 | 0.06 | $4.19\times10^{-6}$ | $3.93\times10^{-6}$ | $2.51\times10^{-7}$ | 0.80 | 4.15 |
| 3% | 0.98 | 0.02 | $1.79\times10^{-6}$ | $1.75\times10^{-6}$ | $3.58\times10^{-8}$ | 0.72 | 3.93 |
| 5% | 0.99 | 0.01 | $8.15\times10^{-5}$ | $8.06\times10^{-5}$ | $8.15\times10^{-7}$ | 0.41 | 4.02 |
| 7% | 0.91 | 0.09 | $4.29\times10^{-5}$ | $3.90\times10^{-5}$ | $3.86\times10^{-6}$ | 0.42 | 4.42 |
| 10% | 0.98 | 0.02 | $4.17\times10^{-6}$ | $4.08\times10^{-6}$ | $8.34\times10^{-8}$ | 0.65 | 3.98 |
| 15% | 0.96 | 0.04 | $2.52\times10^{-6}$ | $2.41\times10^{-6}$ | $1.01\times10^{-7}$ | 0.70 | 3.54 |
| 20% | 0.93 | 0.07 | $7.17\times10^{-7}$ | $6.66\times10^{-7}$ | $5.01\times10^{-8}$ | 0.71 | 2.94 |

parallel alignment of the polymer chains along with clay layers so that the number of polymer chains gets accommodated. Also, the $Li^+$ might interact with the MMMT, and negative charge in the silicate layers provides good dissolution of salt that results in ionic conductivity. This corresponds with the highest salt dissociation in an optimized system [47]. The conductivity is almost four orders higher than the pure blend system. The presence of negative surface charge layer on clay effectively dissociates the salt, and the number of charge carriers contributes to ionic conductivity by taking advantage of sites provided by clay layers. Also, the location of cation inside clay galleries affects the ions migration as obtained by a simulation study and suggests that the $Li^+$ moves faster in the middle of clay galleries as compared to $Li^+$ near silicate surface [48].

For low clay concentration, the polymer chains are in the center of clay galleries, and significant intercalation of polymer chains results in faster cation migration as compared to near clay surface where the cation may get trapped above an octahedral layer of MMMT. In the center of clay galleries, more formation of a favorable environment for cation migration influence the ion dynamics and ease of coordination with polar group promotes faster ion migration, hence ion mobility [25, 49]. Further, addition of nanoclay, $>5\%$ lowering in the electrical conductivity plot, is observed due to restricted ion mobility and unfavorable environment. This may be due to the following reasons: (1) decrease in surface area owing to nanoclay aggregation, (2) blockage of cation percolation path by the clay layers, (3) more chains near clay layer surface, (4) increased viscosity of system and (5) insufficient polymer intercalation.

FTIR confirms the polymer intercalation and it suggests the ease of cation migration while an anion is prevented from an entry in clay galleries. Addition of clay makes tougher anion movement and also supported by the increased viscosity [50]. This is also observed from the FTIR results which show a decrease in a number of charge carriers. The observed enhancement in the electrical conductivity is consistent with the FTIR ion–ion interaction study which infers the enhancement in the fraction of the free ions participating in the conduction. It can be concluded that the addition of an optimum clay content (where balanced attractive forces among polymer, cation and silicate layers occur) is capable to provide a most favorable environment for cation transport and realizes the highest conductivity. This increase in electrical conductivity is clarified further in the forthcoming section by analyzing the dielectric constant, relaxation time, and transport parameters.

### Temperature dependence of ionic conductivity

Figure 9b shows the temperature-dependent impedance plot for the optimized system. It may be noted that the dip in the plot shifts toward lower impedance and implies the enhanced electrical conductivity. Also, the increase in the length of the arc infers the increased double-layer capacitance and confirms the ionic nature of the PNCs with negligible electronic conductivity. The temperature-dependent ionic conductivity is plotted for the same with the highest conductivity (Inset). It is noticed that with an increase in the temperature, conductivity increases and reaches to $1.02\times10^{-4}$ S cm$^{-1}$ (at 60 °C), $1.01\times10^{-3}$ S cm$^{-1}$ (at 100 °C). This enhancement

in the conductivity is attributed to the following reasons: (1) enhancement of the polymer flexibility, (2) faster polymer chain segmental motion, (3) thermal activation of the charge carriers and (4) increased amorphous content and free volume for ion migration. The overall combined effect is that a favorable environment builds up that promotes the cation migration at a faster rate from one coordinating site to another [51].

### Thermal activation energy measurement

Figure 9c shows the temperature-dependent ionic conductivity and are fitted Arrhenius equation to obtain the value of activation energy ($E_a$) from the slope of the linear portion. The solid red line is the Arrhenius fit, and all plots are in good agreement. The activation energy infers the energy linked with the ion dynamics in the polymer matrix and should be lower for the faster ion migration [52]. The activation energy is lowest is for the PNCs film based on PEO–PVC + $LiPF_6$–5% MMMT. For this optimum concentration, the favorable ion migration occurs as compared to the nanoclay-free matrix. This suggests the enhancement of ionic conductivity on clay addition. All the PNCs film shows activation energy in the range 0.4–0.8 eV.

### Differential scanning calorimetry analysis

Figure 10 shows the variation of the glass transition temperature and melting peak against the clay content. It is important to note that the presence of single glass

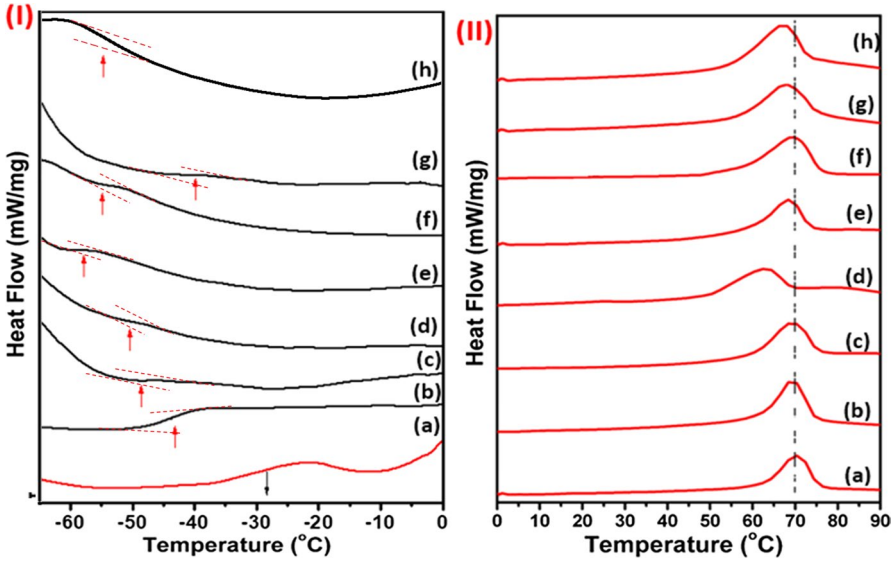


**Fig. 10** DSC curve (I) glass transition temperature, (II) melting peak for various PNC films (a) host blend polymer and (PEO–PVC)–$LIPF_6$ + $x$ wt% MMMT films (b) $x = 0$, (c) $x = 1$, (d) $x = 3$, (e) $x = 5$, (f) 7, (g) $x = 10$, (h) $x = 15$

transition temperature confirms the miscibility of both polymers, and polymer blending occurs which is also in agreement with the FTIR and FESEM results [18, 38]. It may be noted that glass transition temperature shifts toward lower temperature with the addition of the salt, and it indicates the increase in polymer flexibility due to cation coordination with the polymer matrix (Fig. 10I). With the addition of even a low content of MMMT, it shifts further suggests the reduction in polymer recrystallization tendency.

The melting peak in the polymer salt complex (no nanoclay) shifts toward the lower temperature with the addition of nanoclay (Fig. 10II). It indicates the disruption of the covalent bonding between the polymer salt system, and polymer chain becomes more flexible after intercalation in the clay gallery [53]. The crystallinity was obtained using the melting enthalpy, and decrease in crystallinity is evidenced in intercalated polymer nanocomposites as compared to the polymer salt system (Table 4). On the addition of nanoclay, the presence of a negative charge layer on clay galleries easily accommodates the cation-coordinated polymer chains and interactions are modified that disrupts the polymer chain conformation. The overall effect is the enhancement of gallery spacing which makes easier access to the cation for migration. The decrease in crystallinity also evidences that the confined cation-coordinated polymer chains inside clay galleries are more disordered than the polymer chain staying outside [54]. This result is also in perfect agreement with the XRD analysis which confirms the increase in gallery width due to intercalation of polymer chains.

## Electrochemical stability analysis

Another important characteristic of the PNCs is the electrochemical stability window (ESW) and is the maximum voltage limit for safe and trustworthy operation of electrolyte in device applications. The linear sweep voltammetry technique is performed to check the ESW using the cell configuration, SS|PNC|SS in the potential range of −3–3 V at a scan rate of 5 mV/s, where SS refers to stainless steel electrode. Figure 11 shows the LSV for the polymer salt without nanoclay and displays a window of about 3.5 V. Beyond this voltage, the rapid increase in current depicts

**Table 4** Thermal properties ($T_g$, $T_m$, $\Delta H_m$, $X_c$) of the intercalated nanocomposites [(PEO–PVC)–$LIPF_6$ + $x$ wt% MMMT]

| Sample code | $T_g$ (°C) | $T_m$ (°C) | $\Delta H_m$ (J/g) | $X_c$ (%) |
|---|---|---|---|---|
| Pure blend | −30 | 78 | 174 | 92 |
| 0% | −45 | 69 | 110 | 58 |
| 1% | −50 | 69 | 70 | 37 |
| 3% | −53 | 70 | 65 | 34 |
| 5% | −59 | 62 | 53 | 28 |
| 7% | −56 | 68 | 59 | 31 |
| 10% | −42 | 69 | 58 | 30 |
| 15% | −55 | 68 | 71 | 38 |
| 20% | – | 67 | 68 | 36 |

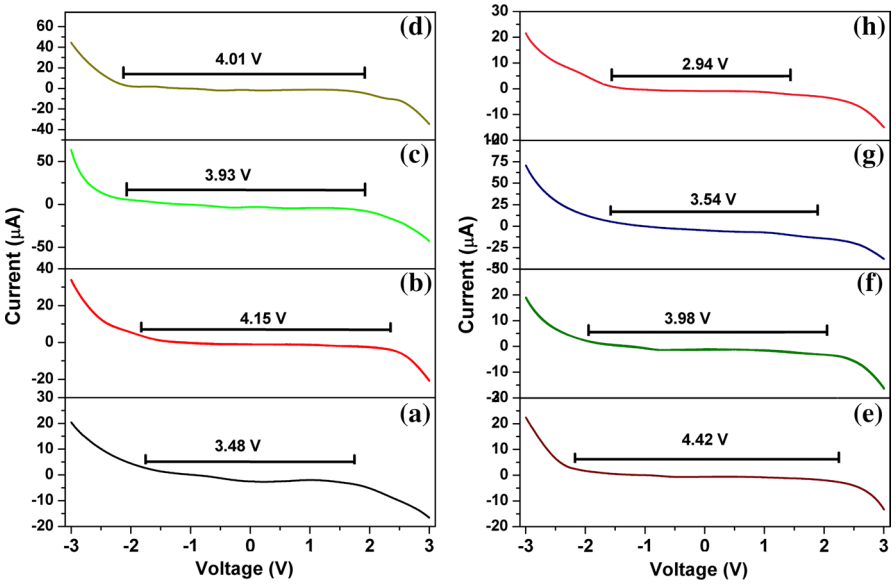


**Fig. 11** Linear sweep voltammetry of polymer nanocomposites with $x$% MMMT, $x$ = a. 0, b. 1, c. 3, d. 5, e. 7, f. 10, g. 15, and h. 20 in the cell configuration SS|PNC|SS

the electrolyte breakdown [55]. After addition of nanoclay in the polymer salt complex, ESW is improved and is in the range of 4–4.5 V. However, at high clay content, voltage window is again reduced and it may be due to poor ionic conductivity. At high clay content, nanoclay is ineffective in improving the electrolyte stability and decrease is observed. The PNC having the highest conductivity exhibits the voltage window of 4.1 V and is large enough for the solid-state Li-ion battery applications (Table 3).

## Transference number analysis

The ion mobility plays a crucial role in the development of new polymer electrolytes. The ion transference number ($t_{ion}$) is obtained using the d.c. polarization method by applying a fixed voltage of 50 mV, and PNC is sandwiched in between the two stainless steel electrodes. The polarization current is monitored as a function of time across the cell configuration and is displayed in Fig. 12 for different clay (% MMMT) contents. All plots show the rapid decrease in current with time, and a steady state is noticed. The initial high current is due to the flow of both ions and electrons ($i_t$), while later on, only electronic/residual current (i.e.,) dominates. The total ionic transport number is in the range 0.91–0.99 and suggests that the ion migration is mainly due to ions [56]. The addition of clay having a negative surface charge layer improves the polymer segmental chain motion and promotes the charge carriers migration which is evidenced by the increased ion transference number. The ion transference number has been used to obtain the ionic and electronic conductivity

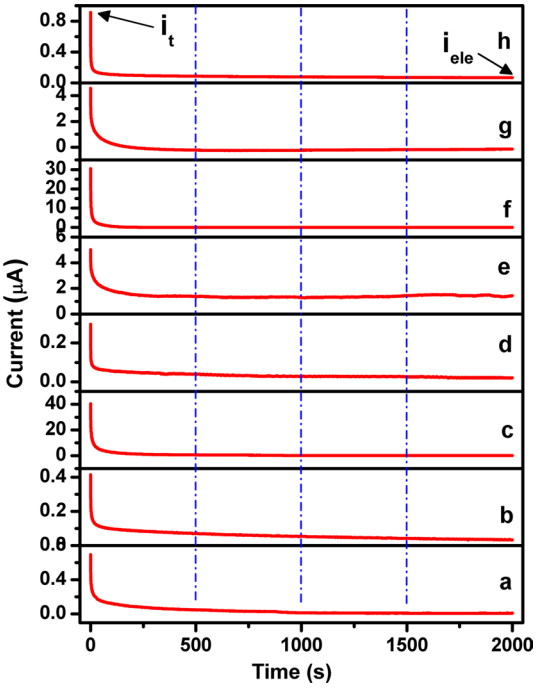


**Fig. 12** Ion transference number measurement of polymer nanocomposites with $x$ wt% MMMT, $x$ = a. 0, b. 1, c. 3, d. 5, e. 7, f. 10, g. 15 and h. 20 in the cell configuration SS|PNC|SS

(Table 3) using the equations, $\sigma_{\text{ionic}} = \sigma_{\text{electrical}} \times t_{\text{ion}}$, and $\sigma_{\text{electronic}} = \sigma_{\text{electrical}} \times t_e$, where $\sigma_{\text{ionic}}, \sigma_{\text{electrical}}$, and $\sigma_{\text{electronic}}$ are the ionic, bulk, and electronic conductivity, respectively.

## Transport parameters

As ion dynamics plays an important role in the section of a PNC for application purpose. So, the three important parameters are explored which directly influence the ionic conductivity ($\sigma$), (1) number density ($n$) of free charge carriers, i.e., ions, (2) ion mobility ($\mu$); degree of ease with which ions pass through media on application of external electrical field, and (3) diffusion coefficient ($D$); ease with which ions pass through media under a concentration gradient. FTIR spectroscopy is used to obtain the transport parameters using the fraction of free ions obtained from deconvoluted FTIR anion ($PF_6^-$) mode and method is reported somewhere [57]. The number density ($n$), mobility ($\mu$), and diffusion coefficient ($D$) of the mobile ions were calculated using the following Eqs. (2)–(4):

$$n = \frac{M \times N_{\text{A}}}{V_{\text{Total}}} \times \text{free ion area}(\%) \tag{2}$$

$$\mu = \frac{\sigma}{ne} \tag{3}$$

$$D = \frac{\mu k_B T}{e} \tag{4}$$

In Eq. (2), M is the number of moles of salt used in each electrolyte, $N_A$ is Avogadro's number ($6.02 \times 10^{23}$ mol$^{-1}$), $V_{Total}$ is the total volume of the solid polymer electrolyte, and $\sigma$ is dc conductivity. In Eq. (3), e is the electric charge ($1.602 \times 10^{-19}$ C), $k_B$ is the Boltzmann constant ($1.38 \times 10^{-23}$ J K$^{-1}$), and $T$ is the absolute temperature in Eq. 4. Table 5 lists the values of $V_{Total}$, free ions (%), $n$, $\mu$, $D$ obtained using the FTIR method [58]. It is observed from Table 4 that the addition of clay in the polymer salt matrix improves the number density of charge carriers, ion mobility and, the diffusion coefficient. It infers the effective role played by the clay layers having negative surface charge layer that facilities the easy migration of cation. The trend in the variation of the conductivity and the transport parameters is similar (Fig. 13).

## Thermogravimetric analysis

Figure 14 shows the thermograms of the polymer salt and polymer salt intercalated nanocomposites. The plot shows three regions. The low-temperature region (< 100 °C) shows minor weight loss for all systems and is associated with the loss of moisture content in the matrix. At high-temperature region (100–200 °C), almost plateau region is observed and suggest the stability of films up to 280 °C. The voltage stability in the intercalated PNCs is improved as compared to the polymer salt complex. The incorporation of nanoclay in the polymer matrix suggests the enhancement of thermal stability. As polymer chains get accommodated inside the clay galleries so it prevents the decomposition of the polymer chains [54]. The clay layers act as a barrier and prevent the polymer decomposition (as shown in inset). In the third region (> 280 °C) region, rapid weight loss is observed and indicates the disruption of the weak bond in the polymer nanocomposites. At very high temperature (> 400 °C), major weight loss is observed that is attributed to the polymer decomposition as well as salt decomposition. It is important to note that the amplitude of the weight loss is lower for the intercalated PNC as compared to polymer salt matrix. At very high nanoclay content weight loss in the low-temperature region is

**Table 5** Values of $V_{Total}$, free ions (%), $n$, $\mu$, $D$ obtained using the FTIR method

| MMMT (wt%) | $V_{Total}$ ($\times 10^{-1}$ cm$^3$) | Free ions area (%) | $n$ ($\times 10^{24}$ cm$^{-3}$) | $\mu$ ($\times 10^{-12}$ cm$^2$ V$^{-1}$ s) | $D$ ($\times 10^{-13}$ cm$^2$ s$^{-1}$) |
|---|---|---|---|---|---|
| 0 | 0.2 | 49.33 | 4.18 | 0.24 | 0.06 |
| 1 | 0.2 | 50.51 | 4.28 | 6.11 | 1.65 |
| 3 | 0.2 | 50.27 | 4.25 | 2.59 | 0.70 |
| 5 | 0.2 | 54.64 | 4.63 | 104 | 28.1 |
| 7 | 0.2 | 54.29 | 4.60 | 58.1 | 15.6 |
| 10 | 0.2 | 53.98 | 4.58 | 5.69 | 1.53 |
| 15 | 0.2 | 53.16 | 4.51 | 3.55 | 0.95 |
| 20 | 0.2 | 52.44 | 4.45 | 1.02 | 0.27 |

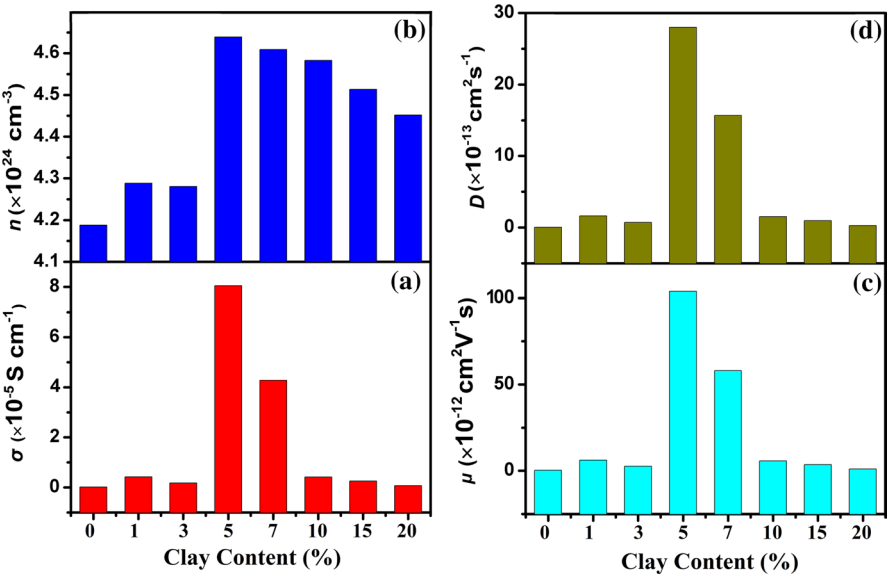


**Fig. 13** Variation of **a** ionic conductivity ($\sigma$), **b** number density ($n$) of free charge carriers, **c** ion mobility ($\mu$), and **d** diffusion coefficient ($D$) for PNC film with different clay content ($x$ wt% MMMT) at room temperature

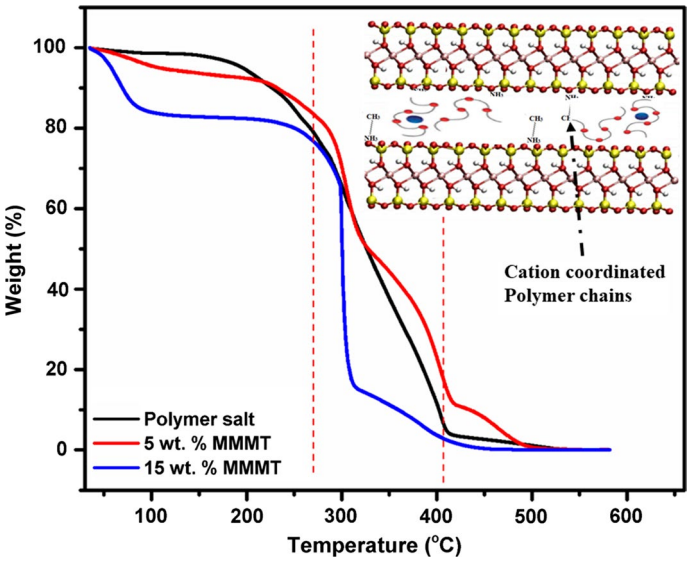


**Fig. 14** Thermograms of the polymer nanocomposite films at 10 °C/min in $N_2$ atmosphere

more and is due to the poor intercalation (some chains stay outside the clay gallery) of polymer chains inside clay galleries [54, 59]. It may be concluded that the intercalated polymer nanocomposites are more thermally stable than the nanoclay-free polymer nanocomposites.

## Dielectric spectroscopy

The dielectric constant is an important property for investigating the ion conducting polymer electrolytes. The high dielectric constant of the polymer matrix infers the better salt dissociation and availability of a more free number of charge carriers. Therefore, the dielectric properties of the polymer blend, blend polymer salt matrix, and intercalated polymer nanocomposite have been evaluated [60]. The frequency dependence of real ($\varepsilon'$) and imaginary part ($\varepsilon''$) of the complex permittivity ($\varepsilon^* = \varepsilon' - j\varepsilon''$) for PEO/PVC–$LiPF_6$–$x$ wt% MMMT solid PNCs is shown in Fig. 15a, b. The real part is dielectric constant ($\varepsilon'$ indicates polarizing ability) and the imaginary part is a dielectric loss ($\varepsilon''$ indicates energy loss in dipoles alignment). Figure 15a shows the high value of the dielectric constant in the low-frequency window for all PNCs and is associated with the dominance of the electrode

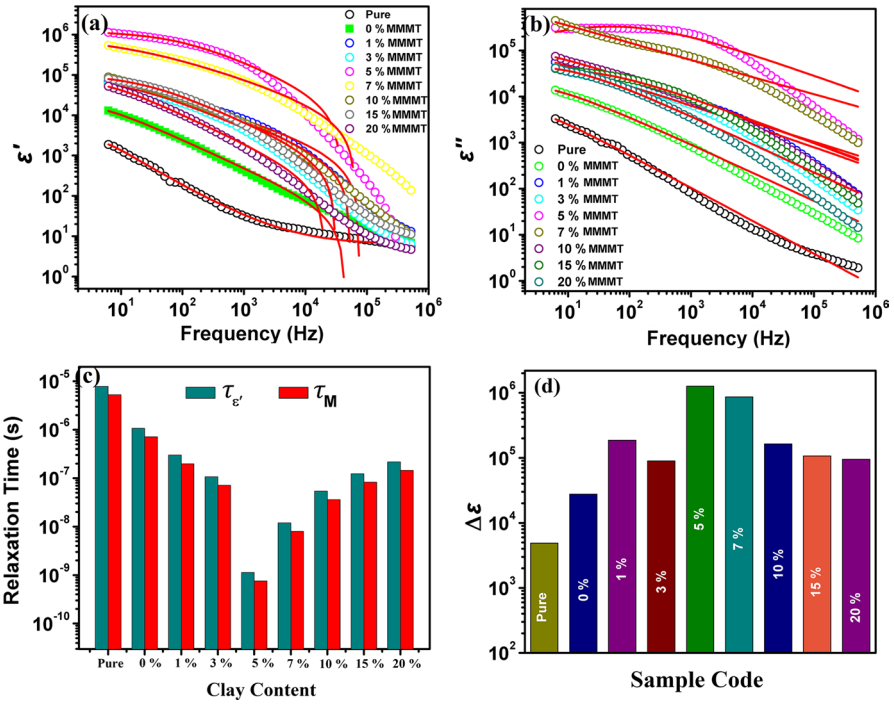


**Fig. 15** Plot of **a** real ($\varepsilon'$), **b** imaginary ($\varepsilon''$) of complex permittivity, **c** variation of relaxation time, **d** dielectric strength for different PNC films ($x$ wt% MMMT) (At RT). Solid lines are the best fit to the experimental data

polarization (EP) or ion accumulation effect. The increase in frequency dielectric constant decreases for all PNCs and is attributed to the periodic reversal of electric field that results in failure of dipoles to follow field direction owing to a short time span. In this region, relaxation process dominates. Figure 15b shows the plot of the imaginary part ($\varepsilon''$) against frequency and depicts the decrease in dielectric loss with an increase in frequency. The dielectric loss is explained by a three-step process during high periodic reversal field. In first step, ion is deaccelerated on change of direction of the field, followed by a steady state in the second step. Then, ion is again accelerated in the opposite direction, and for the zero relaxation time, $\varepsilon''$ is zero, (i.e., for $\omega \to \infty$, $\varepsilon'' \to 0$) [61–63]. It is shown in Fig. 15a that the PNCs with 5 wt% MMMT display the highest value of dielectric constant. This results in good agreement with the deconvoluted anion mode obtained from FTIR and also exhibits the maximum ionic conductivity. It suggests that for the optimum concentration, the increase in a number of charge carriers and faster segmental motion of polymer chain together promotes the faster ion migration. To support this claim, the relaxation time ($\tau_{\varepsilon'}$ and $\tau_m$) are obtained from the fitted parameters.

Figure 15c shows the variation of relaxation time with clay content. Addition of nanoclay lowers the relaxation time and implies the faster polymer chain segmental motion owing to increases flexibility. Figure 15d displays the variation of dielectric strength ($\Delta\varepsilon = \varepsilon_s - \varepsilon_\infty$) with different clay content. It may be noted that dielectric strength is improved as compared to the nanoclay-free PNCs. This enhancement in the dielectric strength indicates the increase in dielectric constant and proper salt dissociation. The PNCs with 5 wt% MMMT indicate the highest value, and these PNCs also show the highest ionic conductivity. At high nanoclay content, dielectric strength decreases due to insufficient polymer chain intercalation into clay galleries that infer the ion pair formation, and hence decrease in dielectric strength. The PNCs with highest ionic conductivity depict the highest dielectric strength and lowest relaxation time.

### Sigma representation

To get further insights into the ion dynamics and to support the impedance data, a new approach sigma representation has been proposed. It comprises of a plot between the real ($\sigma'$) and imaginary part ($\sigma''$) of complex conductivity ($\sigma^*$) with varying frequency [64]. The mathematical expression and physical significance of sigma representation is reported in our previous article [65]. In the plot, low-frequency $x$-intercept gives dc conductivity ($\sigma_o$), and high-frequency $x$-intercept gives $\sigma_\infty$ for $\sigma'' = 0$. The diameter of the semicircle ($D = \sigma_o - \sigma_\infty$) is associated with the relaxation time by the equation $D = [\varepsilon_v(\varepsilon_o - \varepsilon_\infty)]/(2\tau)$, and a large value of diameter suggest the slower relaxation time, hence faster segmental motion of the cation-coordinated polymer chain. Figure 16 shows the semicircle nature that is associated with the ionic conducting nature and with addition of clay in polymer salt complex, increase in the diameter is observed. The highest value is obtained for the 5 wt% MMMT-based polymer nanocomposite and suggests the faster ion migration for this

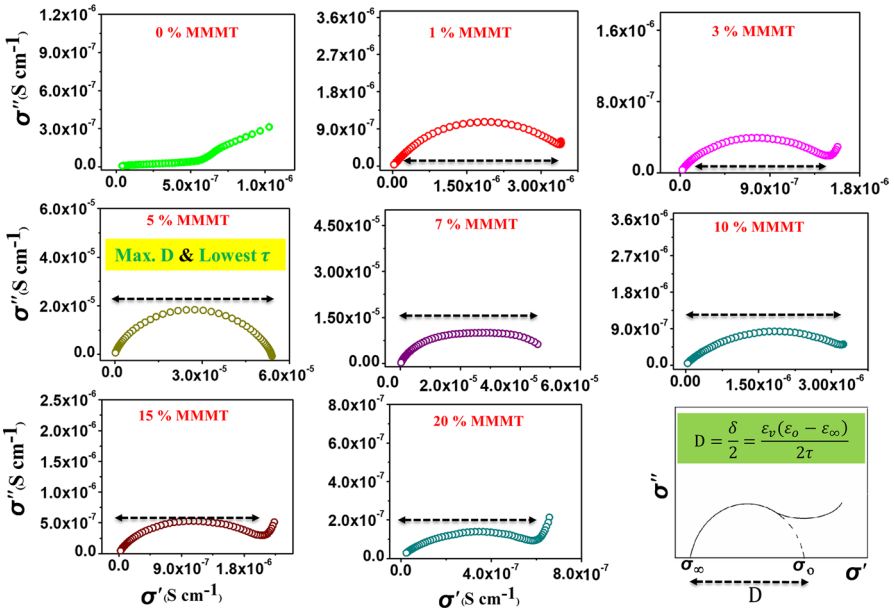


**Fig. 16** Sigma representation ($\sigma''$ vs. $\sigma'$) for the polymer salt matrix with different clay content ($x$% MMMT)

as it is having lowest relaxation time. This is in good agreement with the impedance study, modulus relaxation time, and FTIR analysis.

## Complex conductivity analysis

The frequency dependence of real ($\sigma'$) and imaginary part ($\sigma''$) of the complex conductivity ($\sigma^*$) for PEO/PVC−$LiPF_6$–$x$ wt% MMMT solid PNCs is shown in Fig. 17a and b. The solid red line in the plot is best-stimulated results. Figure 17a depicts

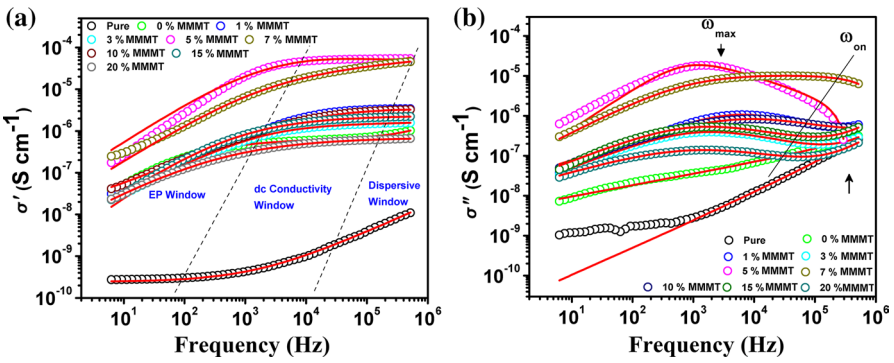


**Fig. 17** Plot **a** real ($\sigma'$), and **b** imaginary ($\sigma''$) of complex conductivity. Solid lines are the best fit to the experimental data

the decrease in frequency in the low-frequency window attributed to the dominance of the electrode polarization (EP) region, an intermediate frequency plateau region corresponding to the dc conductivity and increase in a high-frequency window associated with the dispersive region. The PNCs with 5 wt% shows the maximum dc conductivity and dispersion region lies beyond the measured frequency range. Figure 17b shows the plot of the imaginary part ($\sigma''$) against frequency and gradual increase in frequency at high frequency for pure polymer electrolyte are observed. Now, addition of even a small concentration of clay frequency decreases only up to a certain frequency termed as onset frequency ($\omega_{on}$). This frequency infers the initiation of electrode polarization mechanism, and with further decrease in frequency, maxima in ($\sigma''$) is observed for a particular frequency, i.e., maximum frequency ($\omega_{max}$), associated with complete built-up of polarization [65–72]. The $\sigma''$ again decreases with the decrease in the frequency. It is important to note that both onset and maximum frequency peak lie toward high frequency as compared to other PNCs. This suggests the increase in number of free charge carriers and effective EP effect that enhance the overall ion migration, which is in perfect agreement with the FTIR and impedance study [73].

## The proposed ion transport mechanism

On the basis of the experimental results, an ion transport mechanism was proposed to highlight the role of an individual component of the polymer nanocomposite matrix. The model is the result of the experimental evidence obtained from the FTIR, impedance study, and DSC analysis [74]. Figure 18 shows the proposed model and is split into two sections. The first section highlights the formation of the blend, polymer salt complex, and intercalated polymer nanocomposites (PNC). The second section highlights the role of nanoclay content in the PNC matrix.

Stage 1 depicts the blend formation between the two matrices, i.e., PEO, PVC. The polymer blending is an interesting approach to develop new polymer matrix. It may be observed that the polymer blending occurs between two blends, and most common intersections are hydrogen bonding (shown by dotted line). Besides this, some other interactions exist, i.e., dipole–dipole interactions and ionic interactions. In polymer blend, PEO matrix provides the path for cation migration, while the PVC matrix supports the host matrix by improving mechanical properties. The polymer blend formation was also evidenced by the FESEM and FTIR analysis. In stage 2, when polymer salt is added in the polymer blend, then the salt ($LiPF_6$) get dissociated into cation ($Li^+$) and anion ($PF_6^-$). Now, cation due to Lewis acid nature attracts toward the electron-rich ether group of PEO (i.e., Lewis base), and it results in polymer salt complex formation. Here, two electron-rich sites are available: (1) ether group in PEO chain), (2) chlorine in PVC chain. But, it has been already evidenced by the FTIR that the cation interacts with the ether group rather than electron-rich group of PVC. So, the only possibility here is cation coordination with PEO chain, while anion remains attached with the polymer chain in the immobilized state due to its large size. So, the PEO chain provides the coordinating sites for cation dynamics. In stage 3, when modified nanoclay (MMMT) is added in the polymer salt matrix,

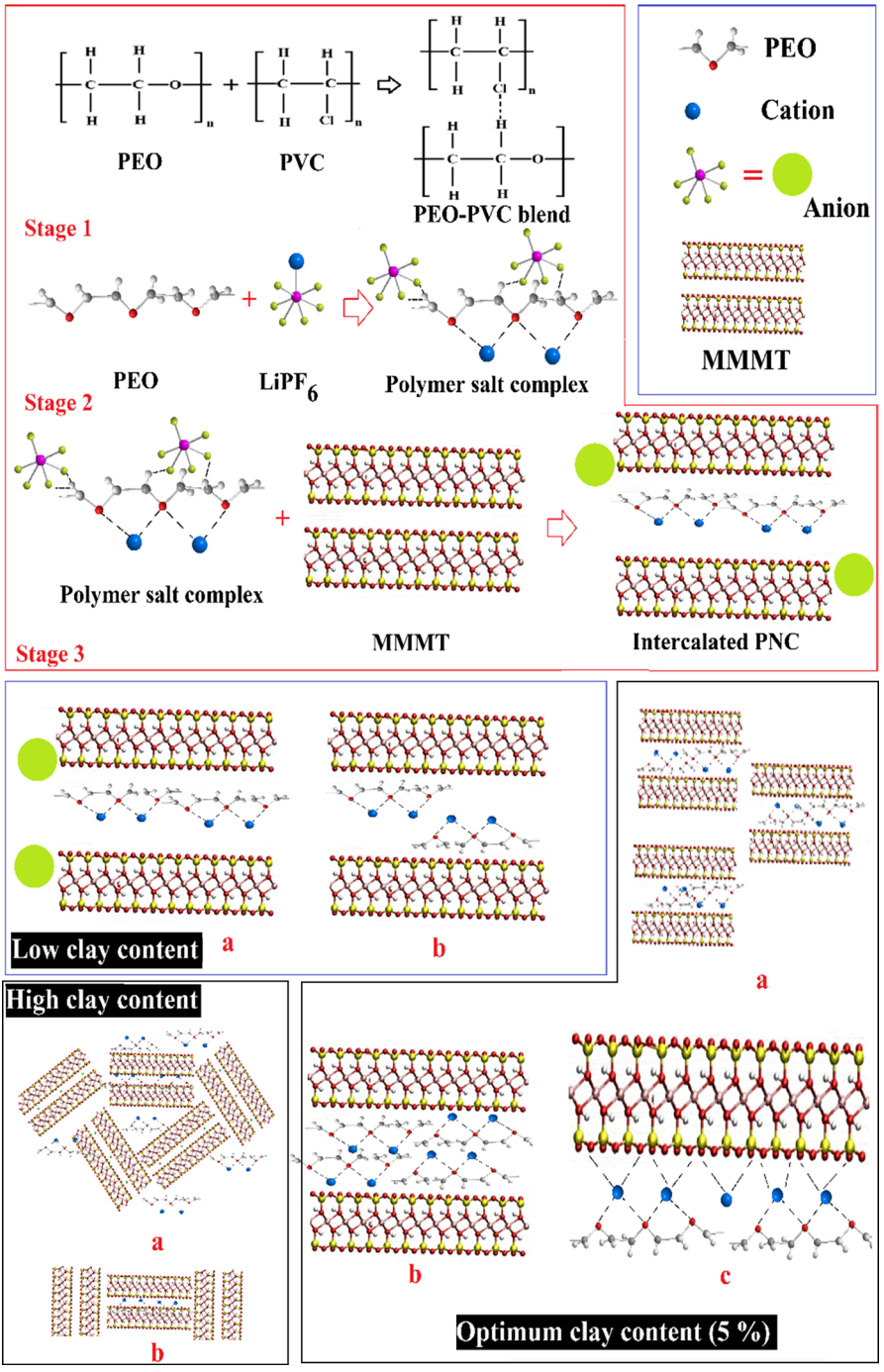


**Fig. 18** Ion transport mechanism in polymer nanocomposites

then cation-coordinated polymer chains get intercalated inside clay galleries. Since clay layer is having a negative surface charge layer (Si–O) in the tetrahedral sheet which provides natural access to polymer chains and accommodates them, this disrupts the Vander wall interactions existing between the clay platelets. The intercalation of the cation-coordinated polymer chains is also confirmed by the XRD and FTIR analysis.

Now, the focus is on understating the role of nanoclay variation in enhancing conductivity. At lower clay content: At the low content of the nanoclay, the cation-coordinated polymer chain intercalation is suitable possibility and anion remains outside the clay gallery. The cation-coordinated polymer chains stay in the gallery center and cation migration is easy (a). Another possibility is indicated by (b) where more polymer chains get accommodated inside clay galleries, and conductivity is enhanced.

Optimum clay content: Now, with an increase in the nanoclay content, balanced interaction between the polymer–salt nanoclay creates a most favorable environment for cation migration. This infers faster ion mobility (a). Figure 18b shows the zoom view of the one clay sheet, and it may be noticed that the polymer chains are negative surface charge layer that holds the cation-coordinated polymer chains, and a number of charge carriers are available owing to the better salt dissociation. Another possibility here is that negative surface charge layers present on the tetrahedral sheet of nanoclay may provide additional sites for the cation migration. The simultaneous occurrence of both possibilities overall enhances the segmental motion of polymer chains. The increased disordered in the intercalated structure also supports cation migration.

High clay content: At higher nanoclay content, decrease in the electrical conductivity as well as transport parameters are observed that is attributed to the following reasons: (1) nanoclay aggregation reduces the surface area, (2) blockage of the ion percolation path by clay layers, (3) increased viscosity of the system. Another reason may be the poor intercalation due to the inhomogeneous distribution of nanoclay in PNC matrix. Now, most of the cation-coordinated polymer chains stay outside the clay gallery and do not participate in conduction due to the tendency of the ion pair formation (a). Also, the reorganization tendency of the polymer chains exists that prevents the segmental motion of the polymer chains.

## Conclusion

We have presented the preparation of a self-standing intercalated polymer nanocomposite (IPNC) films based on blend PEO–PVC/$LiPF_6$/MMMT via standard solution cast method. The structural investigations were performed to explore the polymer intercalation and morphological changes. XRD analysis confirms the reduction in crystallinity and TEM analysis evidences the intercalation of cation-coordinated polymer chain inside clay galleries. The FTIR spectra confirm the formation of polymer–ion nanoclay composite, and an increase in the fraction of free anions and ion pairs simply the effective role played by MMMT. The highest bulk electrical conductivity estimated by the 5 wt% MMMT-doped PNC system and is

about ~ $8.2 \times 10^{-5}$ S $cm^{-1}$ (at RT) and increases to $1.01 \times 10^{-3}$ S $cm^{-1}$ (at 100 °C). The reduction in crystallinity was evidenced by the DSC analysis and is in correlation with the impedance study. The intercalated polymer nanocomposite is stable up to ~ 300 °C. The dielectric analysis indicates the enhancement of dielectric constant with the addition of nanoclay and reduction in relaxation time. The optimized system (with 5 wt% MMT) exhibited the lowest activation energy ($E_a$), lowest melting temperature ($T_m$), which are in close agreement with the relaxation time ($\tau_{\varepsilon'}$ and $\tau_m$). The enhancement in the dielectric constant ($\varepsilon$), ion mobility ($\mu$), and diffusion coefficient ($D$) infers the fast ion dynamics and supports the exhibited electrical conductivity value. The high value of ion transference number (~ 100%) and broad voltage stability window (~ 5 V) of the intercalated polymer nanocomposite suggests their suitability for energy storage/conversion devices.

**Acknowledgements** One of the authors (AA) is thankful to the Central University of Punjab for fellowship.

## References

1. Barbosa JC, Dias JP, Lanceros-Méndez S, Costa CM (2018) Recent advances in poly(Vinylidene fluoride) and its copolymers for lithium-ion battery separators. Membranes 8:45
2. Hong SY, Kim Y, Park Y et al (2013) Charge carriers in rechargeable batteries: Na ions vs. Li ions. Energy Environ Sci 6:2067–2081
3. Yang Q, Zhang Z, Sun XG et al (2018) Ionic liquids and derived materials for lithium and sodium batteries. Chem Soc Rev 47:2020–2064
4. Armand MB (1980) Intercalation electrodes. Materials for advanced batteries. Springer, Boston, pp 145–161
5. Arya A, Sharma AL (2019) Electrolyte for energy storage/conversion (Li+, Na+, Mg2+) devices based on PVC and their associated polymer: a comprehensive review. J Solid State Electrochem 23(4):997–1059
6. Arya A, Sharma AL (2017) Polymer electrolytes for lithium ion batteries: a critical study. Ionics 23:497–540
7. Zhang Z, Shao Y, Lotsch B et al (2018) New horizons for inorganic solid state ion conductors. Energy Environ Sci 11:1945–1976
8. Fenton DE, Parker JM, Wright PV (1973) Complexes of alkali metal ions with poly(ethylene oxide). Polymer 14:589
9. Shriver DF, Bruce PG, In Bruce PG (1995) Solid state electrochemistry. Cambridge University Press, Cambridge, p 95
10. Zhao C, Liu L, Qi X et al (2018) Solid-state sodium batteries. Adv Energy Mater 8:173012
11. Arya A, Sharma AL (2017) Insights into the use of polyethylene oxide in energy storage/conversion devices: a critical review. J Phys D Appl Phys 50:443002
12. Etacheri V, Marom R, Elazari R et al (2011) Challenges in the development of advanced Li-ion batteries: a review. Energy Environ Sci 4:3243–3262
13. Vegge T, Younesi R, Johansson P et al (2015) Lithium salts for advanced lithium batteries: Li–metal, Li–$O_2$, and Li–S. Energy Environ Sci 8:1905–1922
14. Sharma AL, Thakur AK (2010) Improvement in voltage, thermal, mechanical stability and ion transport properties in polymer–clay nanocomposites. J Appl Polym Sci 118:2743–2753
15. Arya A, Sadiq M, Sharma AL (2018) Effect of variation of different nanofillers on structural, electrical, dielectric, and transport properties of blend polymer nanocomposites. Ionics 24:2295–2319
16. Prasanth R, Shubha N, Hng HH, Srinivasan M (2013) Effect of nano-clay on ionic conductivity and electrochemical properties of poly(vinylidene fluoride) based nanocomposite porous polymer membranes and their application as polymer electrolyte in lithium ion batteries. Eur Polym J 49:307–318

17. Sharma AL, Thakur AK (2010) Polymer–ion–clay interaction based model for ion conduction in intercalation-type polymer nanocomposite. Ionics 16:339–350
18. Arya A, Sharma AL (2018) Structural, microstructural and electrochemical properties of dispersed-type polymer nanocomposite films. J Phys D Appl Phys 51:045504
19. Kazim S, Ahmad S, Pfleger J et al (2012) Polyaniline–sodium montmorillonite clay nanocomposites: effect of clay concentration on thermal, structural, and electrical properties. J Mater Sci 47:420–428
20. Shukla N, Thakur AK (2010) Ion transport model in exfoliated and intercalated polymer–clay nanocomposites. Solid State Ion 181:921–932
21. Ray SS, Okamoto M (2003) Polymer/layered silicate nanocomposites: a review from preparation to processing. Prog Polym Sci 28:1539–1641
22. Kim S, Hwang EJ, Jung Y et al (2008) Ionic conductivity of polymeric nanocomposite electrolytes based on poly(ethylene oxide) and organo-clay materials. Colloids Surf, A 313–314:216–219
23. Choudhary S, Sengwa RJ (2012) Ionic conductivity of lithium perchlorate salt in polymeric electrolyte solutions and MMT nano-sheets dispersed colloids. Indian J Eng Mater Sci 19:245–252
24. Chen HW, Chiu CY, Chang FC (2002) Conductivity enhancement mechanism of the poly(ethylene oxide)/modified-clay/$LiClO_4$ systems. J Polym Sci, Part B: Polym Phys 40:1342–1353
25. Chen HW, Lin TP, Chang FC (2002) Ionic conductivity enhancement of the plasticized PMMA/$LiClO_4$ polymer nanocomposite electrolyte containing clay. Polymer 43:5281–5288
26. Feldman D (2015) Polyblend nanocomposites. J Macromol Sci Part A: Pure Appl Chem 52:648–658
27. Fischer H (2003) Polymer nanocomposites: from fundamental research to specific applications. Mater Sci Eng, C 23:763–772
28. Sai Prasanna CM, Austin Suthanthiraraj S (2019) PVC/PEMA-based blended nanocomposite gel polymer electrolytes plasticized with room temperature ionic liquid and dispersed with nano-$ZrO_2$ for zinc ion batteries. Polym Compos. https://doi.org/10.1002/pc.25201
29. Sharma AL, Thakur AK (2011) Polymer matrix-clay interaction mediated mechanism of electrical transport in exfoliated and intercalated polymer nanocomposites. J Mater Sci 46:1916–1931
30. Araujo EM, Leite AMD, da Paz RA et al (2011) Polyamide 6 nanocomposites with inorganic particles modified with three quaternary ammonium salts. Materials 4:1956–1966
31. Fawaz J, Mittal V (2015) Synthesis of polymer nanocomposites: review of various techniques. Wiley, Weinheim, pp 992–1057
32. Fu X, Qutubuddin S (2001) Polymer–clay nanocomposites: exfoliation of organophilic montmorillonite nanolayers in polystyrene. Polymer 42:807–813
33. Ni'Mah YL, Cheng MY, Cheng JH et al (2015) Solid-state polymer nanocomposite electrolyte of $TiO_2$/PEO/$NaClO_4$ for sodium ion batteries. J Power Sources 278:375–381
34. Subban RHY, Arof AK (2004) Plasticiser interactions with polymer and salt in PVC-LiCF $3SO_3$-DMF electrolytes. Eur Polym J 40:1841–1847
35. Cole KC (2008) Use of infrared spectroscopy to characterize clay intercalation and exfoliation in polymer nanocomposites. Macromolecules 41:834–843
36. Sengwa RJ, Dhatarwal P, Choudhary S (2018) Study of time-ageing effect on the ionic conduction and structural dynamics in solid polymer electrolytes by dielectric relaxation spectroscopy. Solid State Ion 324:247–259
37. Ibrahim S, Yassin MM, Ahmad R, Johan MR (2011) Effects of various $LiPF_6$ salt concentrations on PEO-based solid polymer electrolytes. Ionics 17:399–405
38. Anilkumar KM, Jinisha B, Manoj M, Jayalekshmi S (2017) Poly(ethylene oxide) (PEO)—Poly(vinyl pyrrolidone) (PVP) blend polymer based solid electrolyte membranes for developing solid state magnesium ion cells. Eur Polym J 89:249–262
39. Das A, Thakur AK, Kumar K (2013) Exploring low temperature Li+ ion conducting plastic battery electrolyte. Ionics 19:1811–1823
40. Arya A, Sharma AL (2018) Effect of salt concentration on dielectric properties of Li-ion conducting blend polymer electrolytes. J Mater Sci: Mater Electron 29:17903–17920
41. Han SD, Yun SH, Borodin O, Seo D, Sommer DM, Young RD, Henderson WA (2015) Solvate structures and computational/spectroscopic characterization of $LiPF_6$ electrolytes. J Phys Chem C 119:8492–8500
42. Ducasse L, Dussauze M, Grondin J, Lassègues JC, Naudin C, Servant L (2003) Spectroscopic study of poly(ethylene oxide)6: LiX complexes (X = $PF_6$, $AsF_6$, $SbF_6$, $ClO_4$. Phys Chem Chem Phys 5:567–574

43. Chen HW, Chang FC (2001) The novel polymer electrolyte nanocomposite composed of poly(ethylene oxide), lithium triflate and mineral clay. Polymer 42:9763–9769
44. Jonscher AK (1983) Dielectric relaxation in solids. Chelsea Dielectric, London
45. Scrosati B, Croce F, Persi L (2002) Impedance spectroscopy study of PEO-based nanocomposite polymer electrolytes. J Electrochem Soc 147:1718–1721
46. Pritam Arya A, Sharma AL (2019) Dielectric relaxations and transport properties parameter analysis of novel blended solid polymer electrolyte for sodium ion rechargeable batteries. J Mater Sci 54:7131–7155
47. Ghadami A, Taheri Qazvini N, Nikfarjam N (2014) Ionic conductivity in gelatin-based hybrid solid electrolytes: the non-trivial role of nanoclay. J Mater Sci Technol 30:1096–1102
48. Hackett E, Manias E, Giannelis EP (2000) Computer simulation studies of PEO/layer silicate nanocomposites. Chem Mater 12:2161–2167
49. Giannelis EP (1996) Polymer layered silicate nanocomposites. Adv Mater 8:29–35
50. Dam T, Karan NK, Thomas R, Pradhan DK, Katiyar RS (2015) Observation of ionic transport and ion-coordinated segmental motions in composite (polymer–salt–clay) solid polymer electrolyte. Ionics 21:401–410
51. Reddy Polu A, Kumar R (2012) Impedance spectroscopy and FTIR studies of PEG—based polymer electrolytes. E-J Chem 8:347–353
52. Mohamad AA, Mohamed NS, Yahya MZA et al (2003) Ionic conductivity studies of poly(vinyl alcohol) alkaline solid polymer electrolyte and its use in nickel-zinc cells. Solid State Ion 156:171–177
53. Arya A, Sharma AL (2018) Optimization of salt concentration and explanation of two peak percolation in blend solid polymer nanocomposite films. J Solid State Electrochem 22:2725–2745
54. Chrissopoulou K, Andrikopoulos KS, Fotiadou S et al (2011) Crystallinity and chain conformation in PEO/layered silicate nanocomposites. Macromolecules 44:9710–9722
55. Jinisha B, Anilkumar KM, Manoj M, Pradeep VS, Jayalekshmi S (2017) Development of a novel type of solid polymer electrolyte for solid state lithium battery applications based on lithium enriched poly (ethylene oxide)(PEO)/poly (vinyl pyrrolidone)(PVP) blend polymer. Electrochim Acta 235:210–222
56. Fan L, Dang Z, Nan CW, Li M (2002) Thermal, electrical and mechanical properties of plasticized polymer electrolytes based on PEO/P (VDF-HFP) blends. Electrochim Acta 48:205–209
57. Arof AK, Amirudin S, Yusof SZ, Noor IM (2014) A method based on impedance spectroscopy to determine transport properties of polymer electrolytes. Phys Chem Chem Phys 16:1856–1867
58. Bandara TMWJ, Dissanayake MAKL, Albinsson I, Mellander BE (2011) Mobile charge carrier concentration and mobility of a polymer electrolyte containing PEO and $Pr_4N^+ I^-$ using electrical and dielectric measurements. Solid State Ion 189:63–68
59. Salehiyan R, Yussuf AA, Hanani NF, Hassan A, Akbari A (2015) Polylactic acid/polycaprolactone nanocomposite: influence of montmorillonite and impact modifier on mechanical, thermal, and morphological properties. J Elastomers Plast 47:69–87
60. Kanimozhi G, Vinoth S, Harish K, Srinadhu ES, Satyanarayana N (2018) Conductivity and dielectric permittivity studies of KI- based Nanocomposite (PEO/PMMA/KI/$I_2$/ZnO nanorods) polymer solid electrolytes. Polym Compos 40(7):2919–2928
61. Ravi M, Pavani y, Kiran Kumar K, Bhavani S, Sharma AK, Narasimha Rao VVR (2011) Studies on electrical and dielectric properties of PVP:KBr $O_4$ complexed polymer electrolyte films. Mater Chem Phys 131:442–448
62. Jiang X, Zhao X, Peng G, Liu W, Liu K, Zhan Z (2017) Investigation on crystalline structure and dielectric relaxation behaviors of hot pressed poly (vinylidene fluoride) film. Curr Appl Phys 17:15–23
63. Karmakar A, Ghosh A (2012) Dielectric permittivity and electric modulus of polyethylene oxide (PEO)–$LiClO_4$ composite electrolytes. Curr Appl Phys 12:539–543
64. Wei YZ, Sridhar S (1993) A new graphical representation for dielectric data. J Chem Phys 99:3119–3124
65. Arya A, Sharma AL (2018) Structural, electrical properties and dielectric relaxations in $Na^+$-ion-conducting solid polymer electrolyte. J Phys: Condens Matter 30:165402
66. Choudhary S (2017) Dielectric dispersion and relaxations in (PVA–PEO)–ZnO polymer nanocomposites. Phys B 522:48–56
67. Abutalib MM (2019) Effect of zinc oxide nanorods on the structural, thermal, dielectric and electrical properties of polyvinyl alcohol/carboxymethyle cellulose composites. Phys B 557:108–116

68. Arya A, Sharma AL (2019) Tailoring of the structural, morphological, electrochemical, and dielectric properties of solid polymer electrolyte. Ionics 25:1617–1632
69. Casar G, Li X, Malic B, Zhang QM, Bobnar V (2015) Impact of structural changes on dielectric and thermal properties of vinylidene fluoride–trifluoroethylene-based terpolymer/copolymer blends. Phys B 461:5–9
70. Arya A, Sharma AL (2018) Temperature and salt-dependent dielectric properties of blend solid polymer electrolyte complexed with LiBOB. Macromol Res 27(4):334–345
71. García-Bernabé A, Rivera A, Granados A, Luis SV, Compañ V (2016) Ionic transport on composite polymers containing covalently attached and absorbed ionic liquid fragments. Electrochim Acta 213:887–897
72. Das S, Ghosh A (2017) Charge carrier relaxation in different plasticized PEO/PVDF-HFP blend solid polymer electrolytes. J Phys Chem B 121:5422–5432
73. Arya A, Saykar NG, Sharma AL (2019) Impact of Shape (nanofiller vs. nanorod) of $TiO_2$ nanoparticle on free standing solid polymeric separator for energy storage/conversion devices. J Appl Polym Sci 136:47361
74. Arya A, Sadiq M, Sharma AL (2018) Structural, electrical and ion transport properties of free-standing blended solid polymeric thin films. Polym Bull. https://doi.org/10.1007/s00289-018-2645-y

**Publisher's Note** Springer Nature remains neutral with regard to jurisdictional claims in published maps and institutional affiliations.